Inorganic Chemistry
Cite This: Inorg. Chem. XXXX, XXX, XXX−XXX
Article
pubs.acs.org/IC

Phosphatase-like Activity of Tetranuclear Iron(III) and Zinc(II) Complexes

Nityananda Dutta,[†] Shobhraj Haldar,[†] Gonela Vijaykumar,[‡] Suvendu Paul,[†] Asoke Prasun Chattopadhyay,[†] Luca Carrella,[§] and Manindranath Bera*[,†]

[†]Department of Chemistry, University of Kalyani, Kalyani, West Bengal-741235, India

[‡]Department of Chemical Sciences, Indian Institute of Science Education & Research Kolkata, Mohanpur, West Bengal-741246, India

[§]Institut fur Anorganische Chemie und Analytische Chemie, Johannes-Gutenberg Universitat Mainz, Duesbergweg 10-14, D-55128 Mainz, Germany

Supporting Information

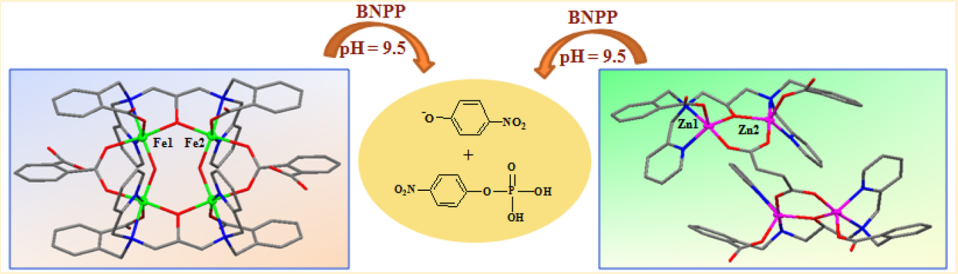

ABSTRACT: Three new tetranuclear iron(III) and zinc(II) complexes, $[Fe_4(cpdp)_2(phth)_2(OH)_2]\cdot 8H_2O$ (**1**), $[Fe_4(cpdp)_2(terephth)_2(OH)_2]$ (**2**), and $[Zn_4(Hcpdp)_2(suc)]Br_2\cdot 12H_2O$ (**3**), have been synthesized as models for the active site of phosphoester hydrolases by utilizing a polydentate ligand, *N*,*N*′-bis[2-carboxybenzomethyl]-*N*,*N*′-bis[2-pyridylmethyl]-1,3-diaminopropan-2-ol (H_3cpdp) in combination with exogeneous phthalate (phth), terephthalate (terephth), and succinate (suc). Single crystal X-ray analyses reveal that the metallic core of complex **1** consists of four distorted octahedral iron(III) ions with average intraligand Fe---Fe separation of 3.656(2) Å, while the structure **3** represents a tetranuclear metallic core containing four distorted trigonal bipyramidal zinc(II) ions with average intraligand Zn---Zn separation of 3.472(2) Å. The molecular structure of complex **2** has been optimized by the DFT method which shows that its core arrangement is similar to that of **1**. Complex **1** has a very interesting centrosymmetric structure that includes two crystallographically equivalent $[Fe_2(cpdp)]^{3+}$ dinuclear units, connected together by a pair of *syn-syn* bridging phthalates and a pair of bridging hydroxides to generate a "dimer of dimers" structural motif. In complex **3**, a succinate group connects two crystallographically equivalent $[Zn_2(Hcpdp)]^{2+}$ dinuclear units in a *syn-syn* bidentate manner forming a "dimer of dimers" structural design. All three complexes show phosphatase-like activity that has been examined in methanol−water (1:1; v/v) using bis(*p*-nitrophenyl) phosphate (BNPP) as model substrate by applying the UV−vis spectrophotometric technique. In each case, the kinetic data have been analyzed by the Michaelis−Menten approach. The order of catalytic efficiency for the conversion of substrate to product follows the trend **1** > **2** > **3** with turnover rates (k_{cat}) of $(2.73 \pm 0.13) \times 10^{-5}$ for **1**, $(1.06 \pm 0.07) \times 10^{-5}$ for **2**, and $(2.33 \pm 0.18) \times 10^{-6}$ s^{-1} for **3**. These k_{cat} values are comparable to, albeit slightly lower than, the values reported for similar iron(III)- and zinc(II)-based model complexes in the literature. DFT calculations have been carried out to support the proposed mechanism for phosphatase-like activity.

INTRODUCTION

Multinuclear units of transition metals are often observed to be the active sites of many enzymatic systems that catalyze the transformations of small molecules relevant to sustainable energy and chemical challenges.[1,2] One of the key advantages of multimetallic systems is the cooperativity of the neighboring metal centers, providing an active binding site for the substrate. Naturally, there has been a long-standing interest in the development of structural as well as functional models of biologically active multimetallo-catalysts, aiming to explore their mechanistic details and modes of actions.[3−7] In this regard, considerable attention has been directed toward the investigation of multinuclear iron(III) and zinc(II) complexes to mimic the active sites that are found in several classes of metalloenzymes. The di- and tetranuclear iron(III) complexes with oxo, hydroxo, and carboxylate bridges are of abundant interest because they can potentially serve as structural and functional models of the active sites of methane monooxygenase, ribonucleotide reductase, purple acid phosphatase, and

Received: May 25, 2018

DOI: 10.1021/acs.inorgchem.8b01441
Inorg. Chem. XXXX, XXX, XXX−XXX

Scheme 1. Synthetic Pathway of the Complexes

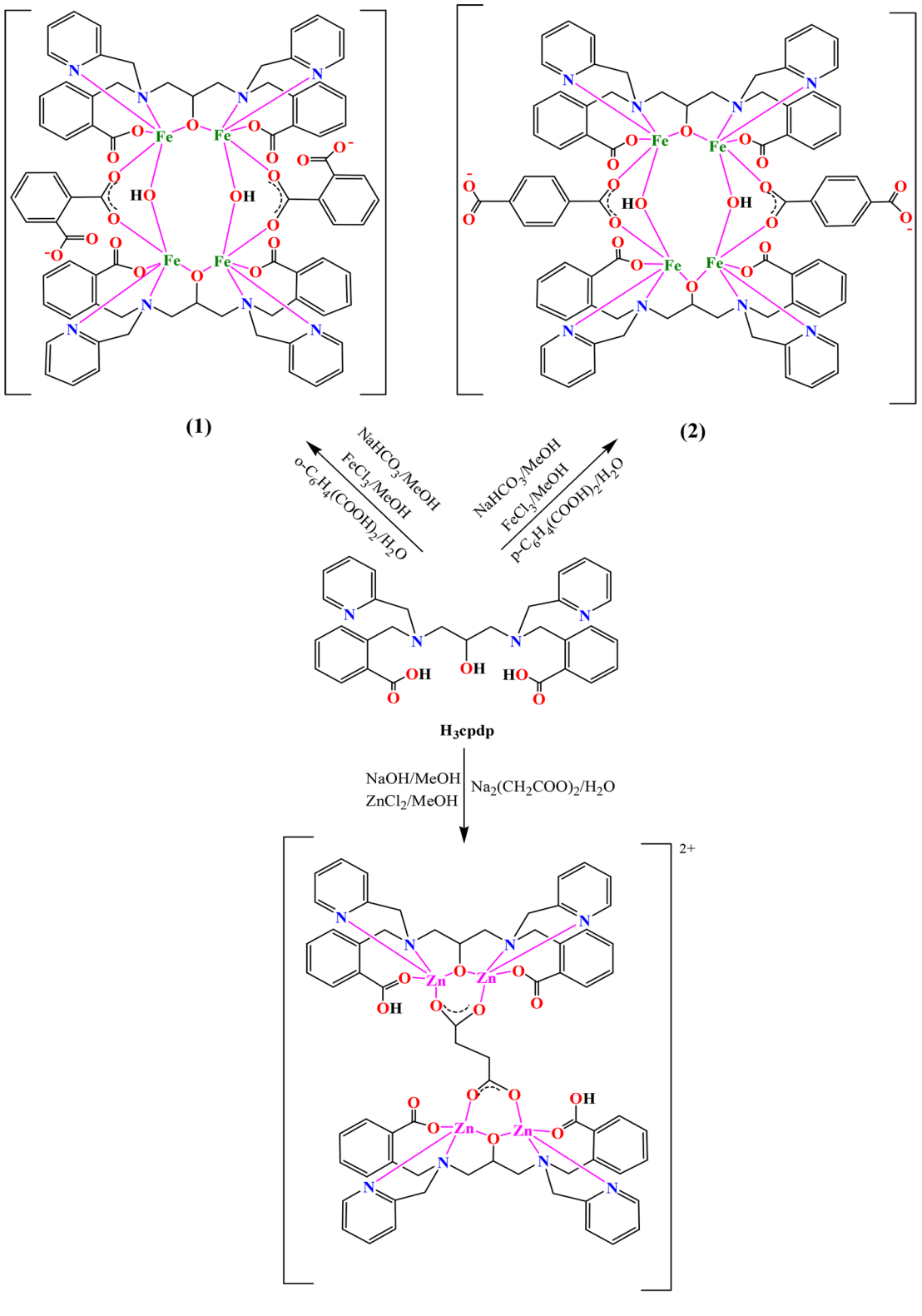

ferritin.[8−14] Again, much of the importance of di- and tetranuclear zinc(II) complexes derives from their activity of metallohydrolases that contain the active sites of leucin aminopeptidase,[15] nuclease P1,[16] kidney bean purple acid phosphatase,[17] alkaline phosphatase,[18] and metallo-β-lactamases.[19]

However, among these various metalloenzymes, purple acid phosphatases (PAPs) belonging to the family of dinuclear metallohydrolases catalyze the hydrolysis of a wide range of

DOI: 10.1021/acs.inorgchem.8b01441
Inorg. Chem. XXXX, XXX, XXX−XXX

phosphoester and amide substrates.[20,21] Generally, PAPs isolated from both plants and animals appear to exist in two forms which can be differentiated by their molecular weight, i.e. a smaller (35 kDa) and a larger (55−60 kDa) form.[22,23] These enzymes have been mostly recognized with two closely spaced heterovalent Fe^{III}-M^{II} (M = Fe, Zn, Mn) ions forming a dimetallic core to perform the hydrolytic reactions. Careful literature studies reveal that PAPs are the most investigated representatives of metallohydrolases and their characteristic purple color in the active site is due to the charge transfer transition between a tyrosine moiety and the iron(III) ion. The biological functions of PAPs include bone metabolism in animals and phosphate acquisition and reactive oxygen species metabolism in plants.[24−26] They have been identified as a beneficial target for the development of original chemotherapeutics for the treatment of osteoporosis and related bone ailments.[21,27] Very recently, Schenk and co-workers[28] have solved and elucidated the high-resolution (1.18 Å) crystal structure of pig PAP which is practically similar to that reported in their previous investigation on this enzyme comprising two sandwiched β-sheets flanked by α-helical segments.[29] The analysis of this high-resolution structure provides insight into the active site and mechanistic features of PAPs. The structure also displays internal symmetry with iron(III)−iron(II) ions bound at the interface between the two halves. As confirmed by the residual electron density map after fitting the oxygen atom, the metal-ion bridging oxygen is likely to be deprotonated. Further, it has been supported by this hydrogen atom located within the hydrogen bond distance of two phosphate oxygen atoms. This hydrogen bond between the μ-OH group and P_i supports the substrate and/or product binding as well as the stabilization of the transition state. The proposed mechanistic model of the PAP catalyzed reaction reported in the literature indicates that the substrate originally binds with the enzyme through the oxygen atom of the phosphate group of the substrate by either monodentate coordination or bridging coordination.[21] The next step includes the nucleophilic attack by a terminally bound iron(III)-hydroxide or an outer sphere water molecule that may be activated.[30]

The present work originates from our recent interest that has been focused on the study of various multinuclear complexes of nickel, copper, and zinc with carboxylate containing polydentate ligands.[31−34] The presence of a number of carboxylate groups with flexible backbones within these ligand systems may offer further opportunities toward the formation of interesting structural frameworks. Very recently, we have explored the binding properties of two isostructural oxo-anions such as phosphate and arsenate within tetranuclear copper(II) and zinc(II) complexes of the ligand H_3cpdp.[35] Previously, a similar amide and carboxylate-based polydentate ligand has been utilized for the preparation of a self-assembled heptanuclear zinc(II) complex displaying unusual amide binding modes.[36] Hendrickson and co-workers[37] have reported the structural and magnetic properties of a similar tetranuclear iron(III) complex with oxo, alkoxo, and carbonato bridges. The formation of a tetranuclear zinc(II) complex and its subsequent conversion into a heptanuclear complex upon further reaction with a zinc salt has been demonstrated by MacLachlan and co-workers.[38] In the present article, we report the synthesis, characterization, X-ray crystal structure, and phosphatase-like activity of three new tetranuclear complexes of iron(III) and zinc(II) with interesting coordination chemistry.

RESULTS AND DISCUSSION

Synthesis and General Characterization. The ligand, H_3cpdp was synthesized and characterized according to our previously published method.[39] The reaction of $FeCl_3$ with H_3cpdp and phthalic acid in 2:1:1 molar ratio in the presence of $NaHCO_3$ in methanol−water offered a light brown solution and the subsequent isolation of well-formed X-ray quality brown crystals of $[Fe_4(cpdp)_2(phth)_2(OH)_2]\cdot 8H_2O$ (**1**) in good yield (~65%), by slow diffusion of diethyl ether in the filtered solution. Similarly, the treatment of a mixture of $FeCl_3$, H_3cpdp, and terephthalic acid in 2:1:1 molar ratio in the presence of $NaHCO_3$ in methanol−water yielded a brown powder complex $[Fe_4(cpdp)_2(terephth)_2(OH)_2]$ (**2**) in ~76% yield. Conversely, the tetranuclear zinc complex $[Zn_4(Hcpdp)_2(suc)]Br_2\cdot 12H_2O$ (**3**) was obtained in good yield (~73%) by carrying out reaction of $ZnCl_2$ with H_3cpdp and sodium succinate in 2:1:0.5 molar ratio in the presence of NaOH in methanol−water. Single crystals of **3** suitable for X-ray analysis were grown by slow diffusion of diethyl ether into a methanol−water solution of the complex. The synthetic procedure of the complexes is illustrated in Scheme 1. The exogeneous phthalate, terephthalate, and succinate ligands used in the present study act as the spacer-cum-bridging units between the two stable dinuclear $[M_2]$ (M = Fe^{III} and Zn^{II}) complexes to produce the "dimer-of-dimers" or tetramers. It is noted that both $NaHCO_3$ and NaOH have a role of proton acceptor to facilitate deprotonation of both the alcoholic and carboxylic groups of the ligand. Characterizations of the complexes have been done using analytical techniques such as elemental analysis, FTIR, UV−vis, room temperature magnetic moment measurements, mass spectrometry, and potentiometric pH titrations. Single crystal X-ray analyses of complexes **1** and **3** established their molecular structures. The room temperature magnetic moment values of 5.81 μ_B/Fe (μ_{total} = 11.62 μ_B/Fe_4) and 5.89 μ_B/Fe (μ_{total} = 11.78 μ_B/Fe_4) for **1** and **2**, respectively, were determined by the Gouy method.[40,41] These values are comparable to those reported for similar iron(III) complexes with μ-OH and bridging acetate groups[42−44] and slightly lower than the spin-only magnetic moment value of 5.91 μ_B/Fe (μ_{total} = 11.82 μ_B/Fe_4) expected for four uncoupled high-spin iron(III) ions, indicating the antiferromagnetic interactions among the iron centers.

The temperature dependence of the magnetic property of complex **1** was investigated on a powdered microcrystalline sample by variable temperature susceptibility measurements. The susceptibility data were collected in the temperature range of 2−300 K using an applied magnetic field of 1 T. Figure S1 (Supporting Information) displays the χ_MT versus T plot for complex **1**. At room temperature a χ_MT-value of 4.77 cm^3 K mol^{-1} was observed, which is significantly lower than the expected value of 17.51 cm^3 K mol^{-1} for four uncoupled spins with $S_1 = S_2 = S_3 = S_4 = {}^5/_2$. By lowering the temperature up to 20 K, a gradual decrease in χ_MT value was observed. Further cooling results in a sharp decrease reaching to a value of 1.55 cm^3 K mol^{-1} at 2 K. This reflects the fact that the magnetic behavior of complex **1** is determined by moderate antiferromagnetic interactions. But a χ_MT-value of 4.77 cm^3 K mol^{-1} obtained at room temperature could not be accomplished by a system with the topology shown in Figure S1, inset (Supporting Information) and four $S = {}^5/_2$. Neither a one J, two J, or four J model is suitable to obtain a satisfactory simulation of the magnetic data. A possible reason for this might be the presence of an underlying coupled paramagnetic impurity. However, by

DOI: 10.1021/acs.inorgchem.8b01441
Inorg. Chem. XXXX, XXX, XXX−XXX

applying the isotropic exchange Hamilton operator: $\hat{H} = -2J_{ij}\Sigma_{ij}\hat{S}_i\hat{S}_j$ and including a weakly coupled paramagnetic impurity, a fitting of the data was obtained with $J_1 = -25$ cm^{-1} and $J_2 = -17$ cm^{-1}, while J_1 represents the interaction via the μ-hydroxo/μ-phthalato bridges and J_2 represents the interaction via the alkoxo bridges. These values of antiferromagnetic coupling constants between the iron(III) ions in complex **1** are comparable to those found in a similar type of dinuclear iron(III) complexes containing analogous Fe---Fe separation and the Fe−O−Fe bridging angle.[45−47]

FTIR and UV−vis Spectroscopy. The FTIR spectra (Figures S2, S3, and S4 of the Supporting Information) of complexes **1**, **2**, and **3** established the presence of endo- and exogeneous carboxylate groups (Table S1, Supporting Information). The relatively higher differences, Δ (Δ = ν_{as}(COO$^-$) − ν_s(COO$^-$)) of 239, 200, and 207 cm^{-1} between the asymmetric and symmetric stretching vibrations for **1**, **2**, and **3**, respectively, are attributed to the monodentate terminal binding mode of carboxylate ligation.[48] The comparatively lower values of Δ at ∼120, 117, and 125 cm^{-1} for **1**, **2**, and **3**, respectively, are indicative of the *syn-syn* bidentate bridging mode (μ_2:η:$^1\eta^1$) of exogeneous phthalate, terephthalate, and succinate groups.[48] Additionally, a strong band at 1607 (**1**), 1610 (**2**), and 1609 (**3**) cm^{-1} is assigned to the ν(C═N) stretching vibrations of the pyridyl functionality of the ligand backbone.

The UV−vis spectra of **1** (Figure S5, Supporting Information) in methanol−water (1:1; v/v) solution (pH ∼ 7.5) show a d−d transition at 508 nm (ε, 590 M^{-1}cm^{-1}), a hydroxo → iron(III) charge transfer transition at 452 nm (ε, 2180 M^{-1}cm^{-1}), and iron(III)-bound ligand-based charge transfer transitions at 261 nm (ε, 10900 M^{-1}cm^{-1}), 228 nm (ε, 14030 M^{-1}cm^{-1}), and 206 nm (ε, 33660 M^{-1}cm^{-1}). The UV−vis spectra of **2** (Figure S6, Supporting Information) are similar to that of **1** with charge transfer transitions at 449 nm (ε, 3910 M^{-1}cm^{-1}), 262 nm (ε, 7430 M^{-1}cm^{-1}), 238 nm (ε, 11800 M^{-1}cm^{-1}), and 203 nm (ε, 34510 M^{-1}cm^{-1}), and a d−d transition at 504 nm (ε, 930 M^{-1}cm^{-1}). In contrast, the UV−vis spectrum of **3** (Figure S7, Supporting Information) has zinc(II)-bound ligand-based $\pi \rightarrow \pi^*$ transitions at 260 nm (ε, 20340 M^{-1} cm^{-1}) and 228 nm (ε, 22550 M^{-1} cm^{-1}).

Description of Molecular Structures of the Complexes. Detailed analyses of molecular structures of the complexes determined by single crystal X-ray crystallography and DFT method are described herein. Whereas the complex **1** crystallizes in a monoclinic system, and the structure was solved in the *C*2/*c* space group, complex **3** crystallizes in the orthorhombic system, and the structure was solved in the *Pnna* space group. Crystallographic parameters of **1** and **3** are summarized in Table 1. Selected bond distances and angles are given in Table 2. Despite our several trials, we did not succeed in preparing single crystals of complex **2** suitable for X-ray diffraction analysis. Therefore, the structure of **2** was optimized by applying the DFT method to find the bond distances, bond angles, and overall geometry around the iron centers. Important bond distances and angles of **2** are summarized in Table 3. In addition, DFT optimization was performed for **1** and **3** for a meaningful comparison of their X-ray structural metric parameters and DFT optimized structures. Significant bond distances and angles obtained from DFT optimization for **1** and **3** are given in Table 4. The structures were optimized without any symmetry restriction. The vibrational frequencies were scrutinized to authenticate the identity of the stationary point, and this was found to be a minimum (without any negative frequency).

Table 1. Crystallographic Parameters for $[Fe_4(cpdp)_2(phth)_2(OH)_2]\cdot 8H_2O$ (1) and $[Zn_4(Hcpdp)_2(suc)]Br_2\cdot 12H_2O$ (3)

	1	3
Empirical formula	$C_{78}H_{84}N_8O_{28}Fe_4$	$C_{66}H_{88}N_8O_{26}Br_2Zn_4$
Formula weight	1804.92	1830.74
Crystal system	Monoclinic	Orthorhombic
Space group	*C*2/*c*	*Pnna*
a, Å	33.110(17)	22.4551(9)
b, Å	14.593(2)	19.2605(9)
c, Å	18.5554(18)	21.0113(8)
α, deg	90	90
β, deg	94.023(15)	90
γ, deg	90	90
Volume, Å^3	8943(5)	9087.3(6)
Z	8	4
Density, Mg/m^3	1.344	1.338
Wavelength, Å	0.71073	1.54184
Temperature, K	293(2)	100(2)
F(000)	3760	3752
Absorption coefficient, mm^{-1}	0.715	2.819
θ range for data collection	1.856° to 28.611°	4.592° to 66.059°
Reflections collected	9972	5500
Independent reflections	4106	4202
R(*F* obsd data) [$I > 2\sigma(I)$][a]	0.1270	0.0948
wR(*F*2 all data)[b]	0.3247	0.2620
Goodness-of-fit on *F*2	0.988	1.064
Largest diff. peak and hole, e/Å^3	+1.442 to −0.744	+1.359 to −0.716

[a] $R1 = \sum||F_o| - |F_c||/\sum|F_o|$. [b] $wR2 = \{\sum[w(F_o^2 - F_c^2)^2]/\sum[w(F_o^2)^2]\}^{1/2}$.

$[Fe_4(cpdp)_2(phth)_2(OH)_2]\cdot 8H_2O$ (1). *X-ray Crystal Structure.* A labeled representation of the tetranuclear unit of complex **1** is shown in Figure 1. The structure comprises a bis(μ-phthalato/μ-hydroxo)-bridged dimer of $[Fe_2(cpdp)]^{3+}$ dimers. Eight lattice waters are cocrystallized with the complex. Formation of complex **1** is accomplished by a self-assembly process where two dinuclear $[Fe_2(cpdp)]^{3+}$ units are brought together onto the bridging phthalato and hydroxo groups. Each iron(III) ion exhibits a distorted octahedral geometry with a N_2O_4 donor set in which N-donors are provided by one tertiary amine and one pyridyl amine group and O-donors are supplied by one bridging alkoxo, one bridging hydroxo, one bridging phthalato, and one nonbridging benzoate group. Similar structural features are observed for other tetranuclear iron(III) complexes reported in the literature.[37,49] Two hydroxo groups act as bridging units between the two dinuclear $[Fe_2(cpdp)]^{3+}$ components through Fe(1)−O(6)−Fe(2) and Fe(1′)−O(6′)−Fe(2′) links with an average bond angle of 138.91(3)°. These bent $Fe_2O_{hydroxo}$ units contain the shorter Fe−O bonds with average distance of 1.855(4) Å which falls within the range (1.80−1.93 Å) reported for other hydroxo-bridged dinuclear Fe(III) complexes.[50−52] Small elongations in the Fe(1)−N(1), Fe(1)−N(2), Fe(2)−N(3), and Fe(2)−N(4) bond distances are found with an average value of 2.190(7) Å. The Fe−$O_{carboxylate}$ and Fe−O_{alkoxo} bond distances are in the range of those previously reported in the literature.[53,54] The average Fe---Fe separation for the μ-alkoxo-bridged dinuclear subunits is 3.656(2) Å, whereas the average Fe---Fe separation across the bis(μ-phthalato/μ-hydroxo)-bridged dinuclear subunits is 3.482(2) Å. It is fascinating to note that the four iron(III) ions in the tetranuclear unit are assembled at the corners of a

DOI: 10.1021/acs.inorgchem.8b01441
Inorg. Chem. XXXX, XXX, XXX−XXX

Table 2. Selected Bond Distances (Å) and Angles (deg) for $[Fe_4(cpdp)_2(phth)_2(OH)_2]\cdot 8H_2O$ (1) and $[Zn_4(Hcpdp)_2(suc)]Br_2\cdot 12H_2O$ (3) Obtained from X-ray Structural Analyses

Bond distances [Å]			
1		**3**	
Fe(1)−O(1)	2.002(5)	Zn(1)−O(1)	1.965(7)
Fe(1)−O(2)	1.974(5)	Zn(1)−O(2)	2.003(6)
Fe(1)−O(6)	1.854(5)	Zn(1)−O(6)	2.043(5)
Fe(1)−O(7)	2.019(6)	Zn(1)−N(1)	2.210(6)
Fe(1)−N(1)	2.225(7)	Zn(1)−N(2)	2.055(7)
Fe(1)−N(2)	2.175(6)	Zn(2)−O(1)	1.937(6)
Fe(2)−O(1)	2.008(5)	Zn(2)−O(4)	1.985(5)
Fe(2)−O(4)	1.989(5)	Zn(2)−O(7)	2.019(6)
Fe(2)−O(6′)	1.865(5)	Zn(2)−N(3)	2.194(8)
Fe(2)−O(8)	2.009(6)	Zn(2)−N(4)	2.054(8)
Fe(2)−N(3)	2.198(7)		
Fe(2)−N(4)	2.163(6)		
Bond angles [deg]			
1		**3**	
O(1)−Fe(1)−O(7)	173.2(2)	O(1)−Zn(1)−O(2)	113.1(3)
O(1)−Fe(1)−N(1)	82.3(2)	O(1)−Zn(1)−O(6)	98.6(2)
O(1)−Fe(1)−N(2)	91.9(2)	N(2)−Zn(1)−N(1)	79.4(3)
O(2)−Fe(1)−O(1)	90.9(2)	O(1)−Zn(1)−N(1)	80.9(3)
O(2)−Fe(1)−O(7)	92.3(2)	O(1)−Zn(1)−N(2)	124.0(3)
O(2)−Fe(1)−N(1)	87.3(2)	O(2)−Zn(1)−N(1)	93.3(3)
O(2)−Fe(1)−N(2)	161.0(2)	O(2)−Zn(1)−N(2)	119.9(3)
O(6)−Fe(1)−O(1)	92.3(2)	O(2)−Zn(1)−O(6)	94.5(2)
O(6)−Fe(1)−O(2)	101.3(2)	O(6)−Zn(1)−N(1)	171.7(2)
O(6)−Fe(1)−O(7)	92.9(2)	O(6)−Zn(1)−N(2)	94.2(2)
O(6)−Fe(1)−N(1)	169.9(2)	N(4)−Zn(2)−N(3)	80.6(3)
O(6)−Fe(1)−N(2)	97.3(2)	O(1)−Zn(2)−N(3)	82.5(3)
O(1)−Fe(2)−O(8)	171.5(2)	O(1)−Zn(2)−N(4)	124.0(3)
O(1)−Fe(2)−N(3)	82.7(2)	O(1)−Zn(2)−O(4)	112.6(2)
O(1)−Fe(2)−N(4)	91.0(2)	O(1)−Zn(2)−O(7)	98.1(3)
O(4)−Fe(2)−O(1)	89.4(2)	O(4)−Zn(2)−N(3)	92.4(2)
O(4)−Fe(2)−O(8)	94.9(2)	O(4)−Zn(2)−N(4)	121.0(3)
O(4)−Fe(2)−N(3)	87.1(2)	O(4)−Zn(2)−O(7)	94.4(3)
O(4)−Fe(2)−N(4)	162.8(2)	O(7)−Zn(2)−N(3)	172.4(2)
O(6′)−Fe(2)−O(1)	93.5(2)	O(7)−Zn(2)−N(4)	92.9(3)
O(6′)−Fe(2)−O(4)	100.9(2)		
O(6′)−Fe(2)−O(8)	92.9(2)		
O(6′)−Fe(2)−N(3)	171.1(2)		
O(6′)−Fe(2)−N(4)	96.2(2)		

rectangle forming a concave shaped octagonal core defined by Fe(1)−O(1)−Fe(2)−O(6)−Fe(1′)−O(1′)−Fe(2′)−O(6′) (Figure 2). A six-membered chelate ring with the −O−C−O− group from the phthalato ligand as well as two iron(III) ions and a μ-hydroxo oxygen atom is formed on either side of the octagonal core. Interestingly, the nonbonded carboxylate arms of the bridging phthalato groups are oriented in a *trans*-fashion with respect to each other. The two benzoate arms and two pyridine arms of the $cpdp^{3-}$ ligand within each dinuclear $[Fe_2]$ subunit are oriented in a *cis*-fashion. The presence of a strong hydrogen bonding interaction between O(6) and O(6′) of the μ-hydroxo groups located at a distance of 2.351(7) Å contributes toward the stabilization of the $[Fe_4]$ core. Furthermore, Figure 3 shows a packing diagram that indicates the carboxylate and pyridyl amine susceptible extensive hydrogen bonding interactions throughout the crystal lattice. These plentiful hydrogen bonding interactions also give the

Table 3. Selected Bond Distances (Å) and Angles (deg) for $[Fe_4(cpdp)_2(terephth)_2(OH)_2]$ (2) Obtained from DFT Calculations

Bond distances [Å]			
Fe(1)−O(8)	1.8400	Fe(2)−O(83)	1.8396
Fe(1)−O(4)	1.9139	Fe(2)−O(6)	1.9132
Fe(1)−O(9)	1.9647	Fe(2)−O(85)	2.0037
Fe(1)−N(12)	2.0088	Fe(2)−N(14)	2.0099
Fe(1)−N(11)	2.0570	Fe(2)−N(13)	2.0647
Fe(1)−O(3)	2.1014	Fe(2)−O(3)	2.1645
Bond angles [deg]			
O(8)−Fe(1)−O(4)	95.652	O(83)−Fe(2)−O(6)	96.591
O(8)−Fe(1)−O(9)	89.930	O(83)−Fe(2)−O(85)	86.182
O(8)−Fe(1)−N(12)	95.613	O(83)−Fe(2)−N(14)	94.770
O(8)−Fe(1)−N(11)	173.767	O(83)−Fe(2)−N(13)	174.368
O(8)−Fe(1)−O(3)	89.706	O(83)−Fe(2)−O(3)	93.647
O(4)−Fe(1)−O(9)	91.248	O(6)−Fe(2)−O(85)	91.987
O(4)−Fe(1)−N(12)	168.418	O(6)−Fe(2)−N(14)	168.466
O(4)−Fe(1)−N(11)	89.148	O(6)−Fe(2)−N(13)	88.649
O(4)−Fe(1)−O(3)	88.489	O(6)−Fe(2)−O(3)	87.843
O(9)−Fe(1)−N(12)	86.084	O(85)−Fe(2)−N(14)	86.782
O(9)−Fe(1)−N(11)	93.948	O(85)−Fe(2)−N(13)	95.728
O(9)−Fe(1)−O(3)	179.529	O(85)−Fe(2)−O(3)	179.744
N(12)−Fe(1)−N(11)	79.809	N(14)−Fe(2)−N(13)	80.074
N(12)−Fe(1)−O(3)	94.250	N(14)−Fe(2)−O(3)	93.422
N(11)−Fe(1)−O(3)	86.440	N(13)−Fe(2)−O(3)	84.460

extra stabilization to the crystal lattice. Additionally, the moderate intramolecular $\pi\cdots\pi$ stacking interactions are detected between the adjacent benzoate−phthalate and phthalate−benzoate because of their face-to-face successive arrangement with the average closest contacts of 3.629 and 3.551 Å, respectively (Figure S8 of the Supporting Information).

DFT Optimized Structure. A depiction of DFT optimized structure of **1** is displayed in Figure S9 of the Supporting Information. The DFT optimized structure shows that the molecular core of **1** is identical to its X-ray crystal structure. Similar to the X-ray structure, the equatorial coordination positions of the distorted octahedral geometry around each iron(III) in **1** are occupied by a tertiary amine nitrogen, a bridging alkoxo oxygen, a bridging hydroxo oxygen, and a bridging phthalate oxygen, and the axial coordination positions are occupied by a pyridyl amine nitrogen and a nonbridging benzoate oxygen. The average Fe−O bond distance in the bent $Fe_2O_{hydroxo}$ units is 1.937 Å which is comparable to that found in the X-ray structure. The Fe−N bond distances for amines and pyridines are in the range of 2.154−2.220 Å which are slightly larger than those obtained from X-ray structure. The average Fe−O bond distances for carboxylates in equatorial and axial positions are 2.010 and 1.974 Å, respectively, which are analogous to those seen in the X-ray structure. The Fe(1)−O(6)−Fe(2) and Fe(1′)−O(6′)−Fe(2′) bond angles formed by two hydroxo groups between the two dinuclear $[Fe_2(cpdp)]^{3+}$ units are 140.785° and 140.796°, respectively, which are slightly higher than those detected from the X-ray structure. The average $Fe-O_{alkoxo}$ bond distances indicate that these bridges are close to symmetric [Fe(1)−O(1), 2.027 Å; Fe(2)−O(1), 2.035 Å]. As observed in the X-ray structure, the comparable average intra- and interdinuclear Fe---Fe separations at 3.729 and 3.472 Å, respectively, are detected.

$[Fe_4(cpdp)_2(terephth)_2(OH)_2]$ (2). *DFT Optimized Structure.* A view of the DFT optimized structure of complex **2** is

DOI: 10.1021/acs.inorgchem.8b01441
Inorg. Chem. XXXX, XXX, XXX−XXX

Table 4. Selected Bond Distances (Å) and Angles (deg) for $[Fe_4(cpdp)_2(phth)_2(OH)_2]\cdot 8H_2O$ (1) and $[Zn_4(Hcpdp)_2(suc)]Br_2\cdot 12H_2O$ (3) Obtained from DFT Calculations

Bond distances [Å]			
1		**3**	
Fe(1)−O(1)	2.027	Zn(1)−O(1)	1.974
Fe(1)−O(2)	1.967	Zn(1)−O(2)	2.011
Fe(1)−O(6)	1.836	Zn(1)−O(6)	2.040
Fe(1)−O(7)	2.016	Zn(1)−N(1)	2.217
Fe(1)−N(1)	2.220	Zn(1)−N(2)	2.056
Fe(1)−N(2)	2.165		
Fe(2)−O(1)	2.035	Zn(2)−O(1)	1.953
Fe(2)−O(4)	1.982	Zn(2)−O(4)	1.975
Fe(2)−O(6′)	1.849	Zn(2)−O(7)	2.024
Fe(2)−O(8)	2.005	Zn(2)−N(3)	2.198
Fe(2)−N(3)	2.193	Zn(2)−N(4)	2.059
Fe(2)−N(4)	2.154		
Bond angles [deg]			
1		**3**	
O(1)−Fe(1)−O(7)	173.7	O(1)−Zn(1)−O(2)	112.69
O(1)−Fe(1)−N(1)	82.464	O(1)−Zn(1)−O(6)	98.4
O(1)−Fe(1)−N(2)	92.1	N(2)−Zn(1)−N(1)	79.7
O(2)−Fe(1)−O(1)	90.6	O(1)−Zn(1)−N(1)	81.0
O(2)−Fe(1)−O(7)	92.3	O(1)−Zn(1)−N(2)	124.5
O(2)−Fe(1)−N(1)	87.2	O(2)−Zn(1)−N(1)	92.7
O(2)−Fe(1)−N(2)	161.4	O(2)−Zn(1)−N(2)	119.7
O(6)−Fe(1)−O(1)	92.3	O(2)−Zn(1)−O(6)	94.5
O(6)−Fe(1)−O(2)	101.0	O(6)−Zn(1)−N(1)	172.2
O(6)−Fe(1)−O(7)	92.4	O(6)−Zn(1)−N(2)	94.2
O(6)−Fe(1)−N(1)	170.3	N(4)−Zn(2)−N(3)	80.5
O(6)−Fe(1)−N(2)	97.2	O(1)−Zn(2)−N(3)	82.7
O(7)−Fe(1)−N(1)	92.1	O(1)−Zn(2)−N(4)	124.3
O(7)−Fe(1)−N(2)	83.2	O(1)−Zn(2)−O(4)	112.3
N(2)−Fe(1)−N(1)	74.9	O(1)−Zn(2)−O(7)	97.9
O(1)−Fe(2)−N(4)	91.3	O(4)−Zn(2)−N(3)	92.2
O(1)−Fe(2)−O(8)	172.2	O(4)−Zn(2)−N(4)	120.9
O(1)−Fe(2)−N(3)	82.7	O(4)−Zn(2)−O(7)	94.3
O(4)−Fe(2)−O(1)	89.1	O(7)−Zn(2)−N(3)	172.5
O(4)−Fe(2)−O(8)	94.8	O(7)−Zn(2)−N(4)	93.0
O(4)−Fe(2)−N(3)	87.2		
O(4)−Fe(2)−N(4)	163.3		
O(6′)−Fe(2)−O(1)	93.5		
O(6′)−Fe(2)−O(4)	100.5		
O(6′)−Fe(2)−O(8)	92.2		
O(6′)−Fe(2)−N(3)	171.4		
O(6′)−Fe(2)−N(4)	96.0		
O(8)−Fe(2)−N(3)	90.7		
O(8)−Fe(2)−N(4)	82.9		
N(4)−Fe(2)−N(3)	76.3		

presented in Figure 4. The DFT optimized structure demonstrates that the molecular core of complex **2** is isostructural to that of complex **1**. As also occurs in **1**, complex **2** can be understood as being self-assembled from two $[Fe_2(cpdp)]^{3+}$ dimers linked by bis(μ-terephthalato/μ-hydroxo) bridges. All four iron centers are in a distorted N_2O_4-octahedral geometry, with N-donors supplied by one tertiary amine and one pyridyl amine group, and O-donors delivered by one bridging alkoxo, one bridging hydroxo, one bridging terephthalato, and one nonbridging benzoate group. As observed in **1**, the $Fe_2O_{hydroxo}$ units are bent with shorter Fe−

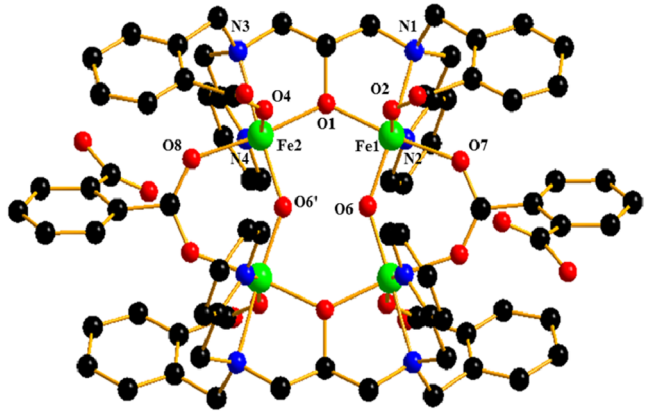

Figure 1. View of the single crystal X-ray structure of complex **1** with atom numbering scheme. Hydrogen atoms are omitted for clarity.

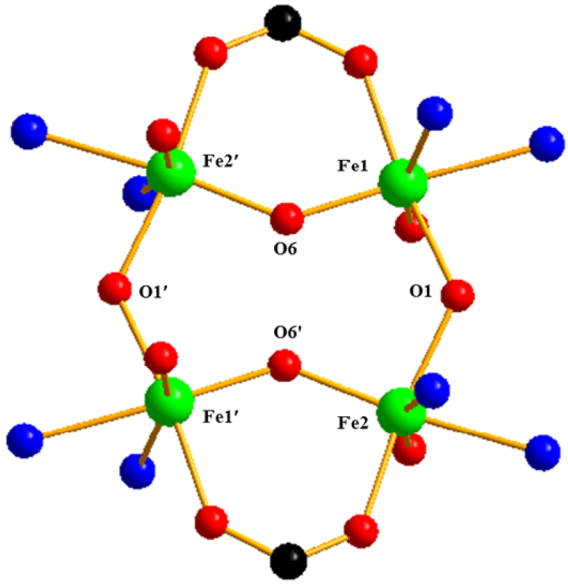

Figure 2. View of the tetranuclear core framework of complex **1** showing a concave shaped octagonal motif.

O bonds at an average distance of 1.839 Å.[50−52] Four iron centers occupy the corners of a quadrilateral feature making a concave shaped octagonal core described by Fe(1)−O(3)−Fe(2)−O(83)−Fe(76)−O(78)−Fe(77)−O(8) (Figure 5). On either side of the octagonal core is a six-membered chelate ring consisting of the −O−C−O− group from the terephthalato ligand as well as two iron(III) ions and a μ-hydroxo oxygen atom sharing the octagonal core. The average Fe---Fe separations within the $cpdp^{3-}$ bridged diiron units and the bis(μ-terephthalato/μ-hydroxo) bridged diiron units are 4.061 and 3.537 Å, respectively. The bridging terephthalato groups are located in such a way that they maximize the T-shaped intramolecular $\pi\cdots\pi$ stacking interactions among themselves and the adjacent aromatic rings of the $cpdp^{3-}$ ligands.[55−57]

$[Zn_4(Hcpdp)_2(suc)]Br_2\cdot 12H_2O$ (3). *X-ray Crystal Structure.* A perspective view of the crystal structure of complex **3** is depicted in Figure 6. The geometry of the tetranuclear core highlighting the arrangement of the zinc(II) ions and the binding modes of succinate is shown in Figure 7. Careful examination of the crystal structure discloses that the complex contains a $[Zn_4(Hcpdp)_2(suc)]^{2+}$ unit, two Br^- ions as counteranions, and 12 lattice waters. Two $[Zn_2(Hcpdp)]^{2+}$

DOI: 10.1021/acs.inorgchem.8b01441
Inorg. Chem. XXXX, XXX, XXX−XXX

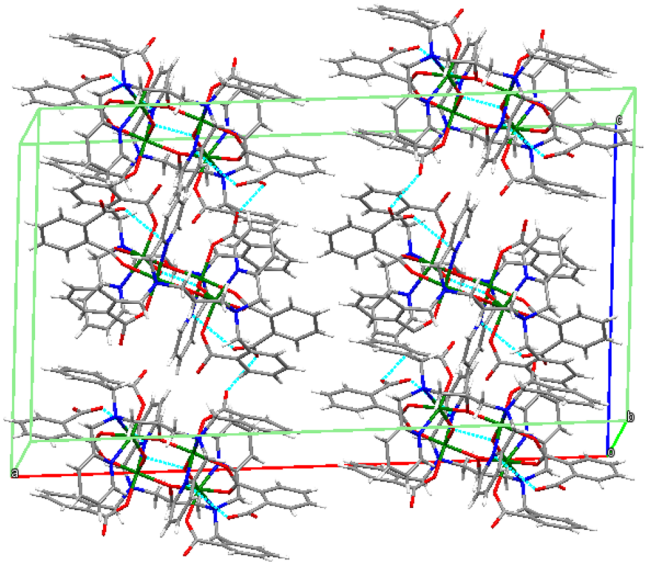

Figure 3. Packing diagram of complex **1** showing hydrogen bonding interactions.

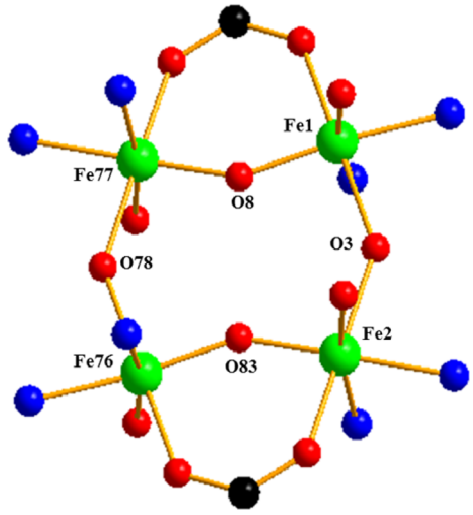

Figure 5. View of the tetranuclear core framework of complex **2** showing a concave shaped octagonal motif.

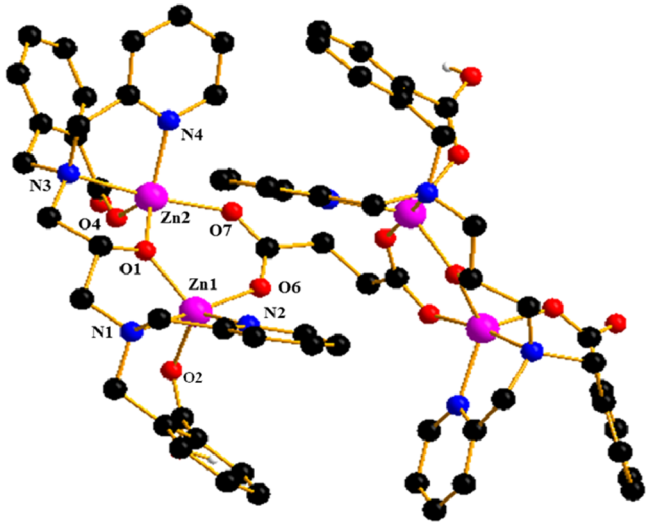

Figure 6. View of the single crystal X-ray structure of complex **3** with atom numbering scheme. Hydrogen atoms are omitted for clarity.

units are linked together by a succinate ligand in a μ_4:η^1:η^1:η^1:η^1 fashion, with each carboxylate group coordinated to both the two zinc(II) ions of one of the dinuclear units in a *syn-syn* mode. Both the two dimers exhibit similar structural arrangements with respect to coordination geometries, bond lengths, and bond angles around the zinc centers. Within each $[Zn_2(Hcpdp)]^{2+}$ unit, the zinc(II) ions are in a grossly distorted trigonal bipyramidal geometry, as confirmed by the values of structural indices ($\tau = 0.795$ for Zn1 and $\tau = 0.806$ for Zn2).[58] The trigonal bipyramidal coordination environment around Zn1 is completed by a bridging alkoxo oxygen (O1), a monodentate benzoic acid oxygen (O2), a tertiary amine nitrogen (N1), a pyridyl nitrogen (N2) of the $cpdp^{3-}$ ligand, and an exogeneous bridging succinate oxygen (O6). Similarly, the trigonal bipyramidal coordination environment around Zn2 consists of a bridging alkoxo oxygen (O1), a monodentate benzoate oxygen (O4), a tertiary amine nitrogen (N3), a pyridyl nitrogen (N4) of the $cpdp^{3-}$ ligand, and an exogeneous bridging succinate oxygen (O7). The longer bond distance of C17−O3 [1.25(1) Å] compared to that of C31−O5 [1.24(1) Å] suggests that O3 is protonated. The deviations of the zinc(II) ions from the basal planes are 0.201 Å (Zn1) and 0.176 Å (Zn2). The Zn−$O_{bridging\ alkoxo}$ bond distances [Zn1−O1, 1.965(6) Å; Zn2−O1,

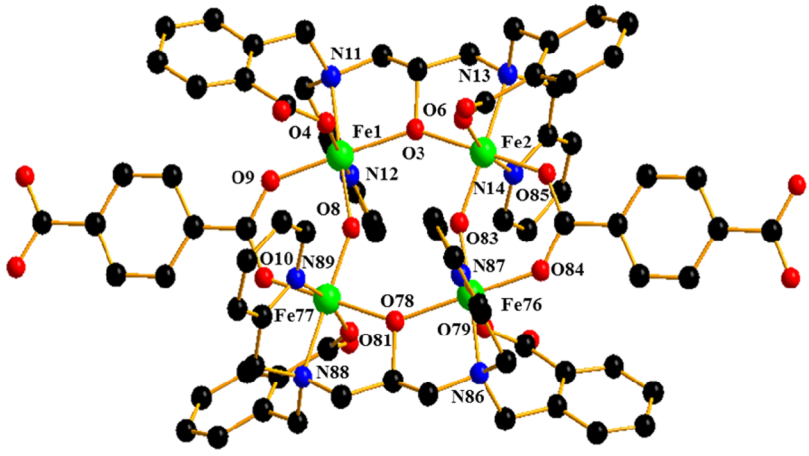

Figure 4. View of the DFT optimized structure of complex **2** with atom numbering scheme. Hydrogen atoms are omitted for clarity.

DOI: 10.1021/acs.inorgchem.8b01441
Inorg. Chem. XXXX, XXX, XXX−XXX

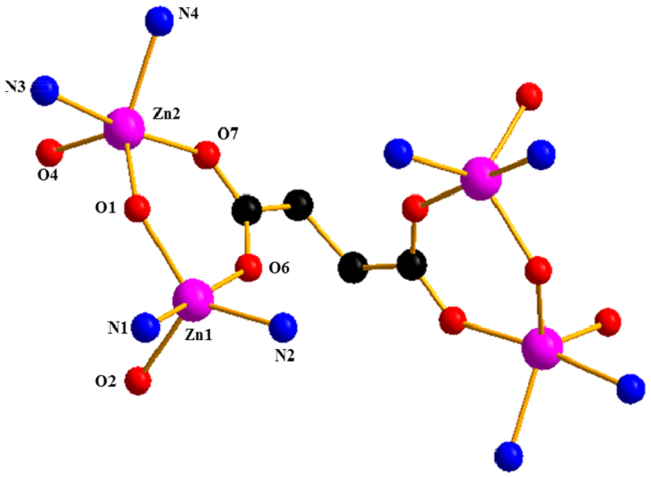

Figure 7. View of the tetranuclear core framework of complex **3**.

1.937(5) Å] are within the range of those reported earlier,[35,59] and the values show that the Zn−O alkoxo bridge is asymmetric. The Zn−$O_{bridging\ carboxylate}$ bond distances [Zn1−O6, 2.042(5) Å; Zn2−O7, 2.020(7) Å] specify that the Zn−O succinate bridge is close to symmetric. The average intradimeric Zn---Zn separation is 3.472(2) Å, and the interdimeric Zn---Zn separation is 6.766(2) Å. Nevertheless, the framework integrity of the tetranuclear core is cleverly maintained by the extensive hydrogen bonding interactions formed among the lattice waters, benzoate, and benzoic acid groups throughout the crystal lattice (Figure S10 of the Supporting Information). It may be noteworthy to say that the moderate intramolecular $\pi\cdots\pi$ stacking interactions can be considered for complex **3** due to face-to-face sequential arrangement of benzoate-pyridyl-pyridyl-benzoate rings (Figure S11 of the Supporting Information). Such interactions have been observed between the adjacent benzoate-pyridyl, pyridyl−pyridyl, and pyridyl-benzoate rings, with average closest contacts of 3.755, 3.955, and 3.755 Å, respectively.

DFT Optimized Structure. The DFT optimized structure of **3** is shown in Figure S12 of the Supporting Information. As observed in the X-ray crystal structure, the succinate group acts as a linker between two $[Zn_2(Hcpdp)]^{2+}$ units through a $\mu_4{:}\eta^1{:}\eta^1{:}\eta^1{:}\eta^1$ bridging coordination mode, with each carboxylate group bridged to two zinc(II) ions of one of the dinuclear units in a *syn-syn* fashion. Analogous to the X-ray structure, two zinc(II) ions within the $[Zn_2(Hcpdp)]^{2+}$ unit display a five-coordinate distorted trigonal bipyramidal geometry with trigonality factor (τ) 0.795 and 0.803.[58] The trigonal bipyramidal geometry around the Zn(1) center is defined by a pyridyl nitrogen (N2), a bridging alkoxo oxygen (O1), and a monodentate benzoic acid oxygen (O2) atom at the equatorial position, and a tertiary amine nitrogen (N1) and a bridging succinate oxygen (O6) atom at the axial position. Similarly, the trigonal bipyramidal geometry around the Zn(2) center is completed by a pyridyl nitrogen (N4), a bridging alkoxo oxygen (O1), and a monodentate benzoate oxygen (O4) atom at the equatorial position, and a tertiary amine nitrogen (N3) and a bridging succinate oxygen (O7) atom at the axial position. The longer C17−O3 [1.317 Å] versus shorter C31−O5 [1.252 Å] bond distances are comparable to those observed in the X-ray crystal structure indicating the O3 is protonated. The average intra- and interdinuclear Zn---Zn separations are 3.500 and 7.087 Å, respectively, a little larger than those acquired from the X-ray crystal structure.

Mass Spectrometry. Furthermore, the ESI-MS of **1**, **2**, and **3** were recorded and analyzed in a methanol−water mixture (pH ∼ 7.5) after dissolving the complexes to gain insight into their structural behavior in solution. The positive ion mode ESI-MS of the complexes are given in Figures S13, S14, and S15 of the Supporting Information. The mass spectrum of **1** (Figure S13(a)) contains three signals at m/z = 1661 (100%), 739 (63%), and 665 (28%) corresponding to the $[Fe_4(cpdp)_2(phth)_2(OH)_2{+}H]^+$, $[Fe_4(cpdp)_2(OH)_4(CH_3OH)_3(H_2O)]^{2+}$, and $[Fe_4(cpdp)_2(O)_2]^{2+}$ species, respectively. For the molecular ion at m/z = 1661, the experimentally obtained and simulated isotope distribution patterns are displayed in Figure S13(b). The examination of the distribution patterns for the experimentally obtained and the simulated data indicates an excellent agreement with one another. Similarly, the mass spectrum of **2** (Figure S14(a)) obtained under same experimental conditions consists of two signals corresponding to the $[Fe_4(cpdp)_2(terephth)_2(OH)_2{+}H]^+$ and $[Fe_4(cpdp)_2(O)_2]^{2+}$ species at m/z = 1661 (8%) and 665 (100%), respectively. The experimentally obtained and simulated isotope distribution patterns for the molecular ion peak at m/z = 1661 are shown in Figure S14(b). Similarly, under identical experimental conditions, the ESI-MS recorded for **3** contains signals matching to the $[Zn_4(cpdp)_2(suc)(H_2O)_2{+}H]^+$, $[Zn_2(cpdp)(H_2O)(CH_3OH)_4]^+$, and $[Zn_2(cpdp)(H_2O)_3(CH_3OH)]^+$ species at m/z = 1483 (4%), 811 (100%), and 751 (60%), respectively (Figure S15(a)). As displayed in the representative Figure S15(b), the experimentally found and the simulated isotope distribution patterns for $[Zn_2(cpdp)(H_2O)(CH_3OH)_4]^+$ at m/z = 811 are in good agreement with one another. Hence, the ESI-MS results of the metal complexes clearly establish that the $cpdp^{3-}$ ligands remain firmly coordinated to the metal centers with tetranuclear identity of **1** and **2** and dinuclear identity of **3** in solution.

Potentiometric pH Titration and Species Distribution. The pH dependence of the species distribution is crucial for understanding any hydrolytic mechanism in solution. Therefore, potentiometric pH titrations were conducted to evaluate the pK_a values of the coordinated water molecules in **1**, **2**, and **3** in methanol−water (1:1; v/v) solution, with the ionic strength maintained at I = 0.1 M $NaNO_3$. The pH-dependent potentiometric titration curves for **1**, **2**, and **3** are illustrated in Figures 8, S16, and S17, respectively. The results obtained for the complexes show that the neutralization takes place with 2 mol of NaOH per mol of each complex in the pH range of 3−11. The two deprotonation steps are likely to happen at the two coordinated water molecules. Consequently, we have calculated two deprotonation constants by considering the potentiometric pH titration data. The observed pK_a values of the coordinated water molecules are 8.37 ± 0.33 and 9.22 ± 0.36 for **1**, 8.58 ± 0.51 and 9.72 ± 0.58 for **2**, and 7.74 ± 0.54 and 9.65 ± 0.67 for **3** (Table 5). When compared with the pK_a values of model di- and tetranuclear iron(III) complexes reported in the literature, slightly higher pK_a values for **1** and **2** have been determined.[60,61] On the other hand, the pK_a values for **3** show the expected trends are fairly close in magnitude when compared with the pK_a values of the previously published model di- and tetranuclear zinc(II) complexes.[62,63] Determination of these pK_a values indicates that the deprotonation of metal-bound water molecules occurs at alkaline pH with the simultaneous formation of metal-bound hydroxo species. Therefore, based on the potentiometric pH titration data, we are inclined to consider that the two pK_a values

DOI: 10.1021/acs.inorgchem.8b01441
Inorg. Chem. XXXX, XXX, XXX−XXX

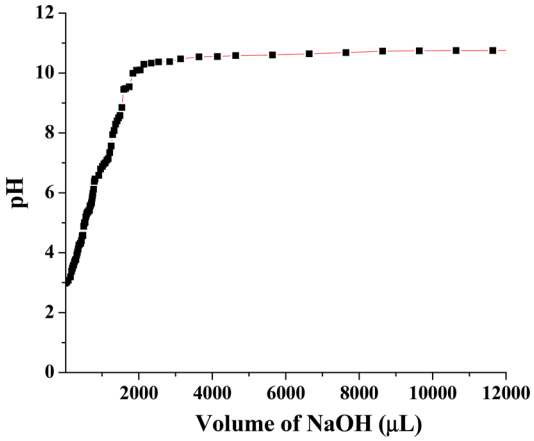

Figure 8. Plot for the potentiometric pH titration achieved by titrating complex **1** with 0.01 M NaOH. The experimental points (black squares) are in good agreement with the theoretical curve (red line).

Table 5. Stability Constants and pK_a Values for the Complex Species

Species	log β	pK_a
$[Fe_4(cpdp)_2(phth)_2(OH)_2]$ (**1**)	29.72	
$[Fe_4(cpdp)_2(H_2O)_4(OH)_2]^{4+}$ (**4**)	24.74	
$[Fe_4(cpdp)_2(H_2O)_3(OH)_3]^{3+}$ (**5**)	17.59	8.37 ± 0.33
$[Fe_4(cpdp)_2(H_2O)_2(OH)_4]^{2+}$ (**6**)	9.22	9.22 ± 0.36
$[Fe_4(cpdp)_2(terephth)_2(OH)_2]$ (**2**)	31.29	
$[Fe_4(cpdp)_2(H_2O)_4(OH)_2]^{4+}$ (**4**)	25.64	
$[Fe_4(cpdp)_2(H_2O)_3(OH)_3]^{3+}$ (**5**)	18.30	8.58 ± 0.51
$[Fe_4(cpdp)_2(H_2O)_2(OH)_4]^{2+}$ (**6**)	9.72	9.72 ± 0.58
$[Zn_2(cpdp)(H_2O)_2]^{2+}$ (**7**)	22.83	
$[Zn_2(cpdp)(H_2O)(OH)]$ (**8**)	17.39	7.74 ± 0.54
$[Zn_2(cpdp)(HO)(OH)]^-$ (**9**)	9.65	9.65 ± 0.67

for complexes **1** and **2** are owing to the conversion of "$Fe^{III}_2(H_2O)_2$-$Fe^{III}_2(H_2O)_2$" to "$Fe^{III}_2(H_2O)_2$-$Fe^{III}_2(H_2O)$-(OH)" species (pK_{a1}) and "$Fe^{III}_2(H_2O)_2$-$Fe^{III}_2(H_2O)(OH)$" to "$Fe^{III}_2(H_2O)(OH)$-$Fe^{III}_2(H_2O)(OH)$" species (pK_{a2}), and those for complex **3** are due to the conversion of "$Zn^{II}(H_2O)$-$Zn^{II}(H_2O)$" to "$Zn^{II}(H_2O)$-$Zn^{II}(OH)$" species (pK_{a1}) and "$Zn^{II}(H_2O)$-$Zn^{II}(OH)$" to "$Zn^{II}(OH)$-$Zn^{II}(OH)$" species (pK_{a2}) (Scheme 2). In addition, the titration curves allowed the calculation of the stability constants of **1**, **2**, and **3** over the entire pH range of 3−11 and the values are given in Table 5. Again, as seen in the species distribution diagrams in Figures 9 and S18, both complexes **1** and **2** are present in solution, predominantly in their corresponding tetrameric forms, in the pH range of 5−11. On the other hand, complex **3** exists mostly in its corresponding dimeric form in solution, in the pH range of 5−11 (Figure 10). For all three complexes, the potentiometric titrations were restricted to a pH ∼ 11, as the substantial precipitation of ferric hydroxide and zinc hydroxide was observed above pH ∼ 11. Hence, basically the formation of tetrameric "$Fe^{III}_2(H_2O)(OH)$-$Fe^{III}_2(H_2O)(OH)$" for **1** and **2** and dimeric "$Zn^{II}(OH)$-$Zn^{II}(OH)$" for **3** has been proposed as the active species in solution during phosphoester hydrolysis.

Phosphatase-like Activity. The phosphatase-like activity[64−66] of complexes **1**, **2**, and **3** was investigated in methanol−water (1:1; v/v) at pH ∼ 9.5 using bis(*p*-nitrophenyl) phosphate (BNPP). The initial rate was measured by spectrophotometrically following the increase in absorbance of the liberated *p*-nitrophenolate anion at 400 nm under the pseudo-first-order reaction conditions. The pH dependence of the reactivity of the complexes is displayed in Figure 11. For all three complexes, the initial rate shows a sigmoidal dependence on the pH, characteristic of a kinetic process controlled by an acid−base equilibrium. The rate versus pH plots reveal that the rate is strongly influenced by the pH of the reaction mixture, reaching a modest maximum rate at pH ∼ 9.5. The data of pH dependence of the rate for **1**, **2**, and **3** has been fitted separately to estimate the kinetic pK_a values using the following equation derived for diprotic systems.[61] Here, v_0 is the

$$v_0 = \frac{v_{max}\left(1 + \frac{\gamma K_{a2}}{[H^+]}\right)}{1 + \frac{[H^+]}{K_{a1}} + \frac{K_{a2}}{[H^+]}}$$

initial reaction rate and v_{max} is the maximum reaction rate. The factor γ is the ratio of limiting rate at high pH and the rate at optimum pH. The values of K_a obtained are the protonation equilibrium constants between the two relevant active species. Two pK_a values obtained for each complex (pK_{a1} = 8.48 ± 0.42 and pK_{a2} = 9.48 ± 0.47 for **1**; pK_{a1} = 8.49 ± 0.25 and pK_{a2} = 9.52 ± 0.28 for **2**; pK_{a1} = 8.49 ± 0.33 and pK_{a2} = 9.49 ± 0.75 for **3**) are in good agreement with the pK_a values determined by potentiometric titrations (pK_{a1} = 8.37 ± 0.33 and pK_{a2} = 9.22 ± 0.36 for **1**; pK_{a1} = 8.58 ± 0.51 and pK_{a2} = 9.72 ± 0.58 for **2**; pK_{a1} = 7.74 ± 0.54 and pK_{a2} = 9.65 ± 0.67 for **3**). The excellent agreement between the potentiometric and kinetic pK_a values supports the proposal that the deprotonation of coordinated water molecules is required to produce the catalytically active Fe^{III}- and Zn^{II}-coordinated hydroxo species "$Fe^{III}_2(H_2O)(OH)$-$Fe^{III}_2(H_2O)(OH)$" and "$Zn^{II}(OH)$-$Zn^{II}(OH)$", respectively (Scheme 2).

The dependence of the initial rate on complex and substrate concentrations was examined to explain the reactivity. For all three complexes, the rate of hydrolysis is linearly dependent on the complex concentrations at pH ∼ 9.5 as revealed by the kinetics data (Figure 12). The determination of the initial rates as a function of substrate concentrations shows saturation kinetics with Michaelis−Menten-like behavior. A first-order dependence on the substrate concentrations was established at lower concentration of substrate, and the saturation kinetics were observed at higher concentration of substrate. We have obtained the Lineweaver−Burk (double reciprocal) plots and the values of various kinetic parameters k_{cat}, K_m, V_{max}, k_{cat}/K_m, and k_{cat}/k_{uncat} by applying the Michaelis−Menten approach of enzyme kinetics and using the equation $1/V = (K_m/V_{max})(1/[S]) + 1/V_{max}$. The rate versus substrate concentration plots and the Lineweaver−Burk plots for the complexes are shown in Figures 13, S19, and S20. The kinetic parameters obtained under the specified experimental conditions from these plots are summarized in Table 6. The turnover rates (k_{cat}) for complexes **1**, **2**, and **3** are calculated to be (2.73 ± 0.13) × 10^{-5}, (1.06 ± 0.07) × 10^{-5}, and (3.05 ± 0.18) × 10^{-6} s^{-1}, respectively. Under similar experimental conditions but in the absence of any catalyst, the hydrolytic cleavage of BNPP in methanol−water (1:1; v/v) has been performed. Compared to the uncatalyzed reaction, complexes **1**, **2**, and **3** accelerate the turnover rates of 2.93 × 10^2, 1.13 × 10^2, and 3.28 × 10^1 fold, respectively, at pH ∼ 9.5 over the background reaction.

Comparing these k_{cat} values of **1**−**3** with the values reported for some dimetallic iron(III),[60,67] iron(III)−zinc(II),[68] and zinc(II)[69,70] model complexes, one can say that the analogous catalytic rates and efficiency are observed for the present

DOI: 10.1021/acs.inorgchem.8b01441
Inorg. Chem. XXXX, XXX, XXX−XXX

Scheme 2. Conversion of Complexes (a) 1 and 2 and (b) 3, in Solution

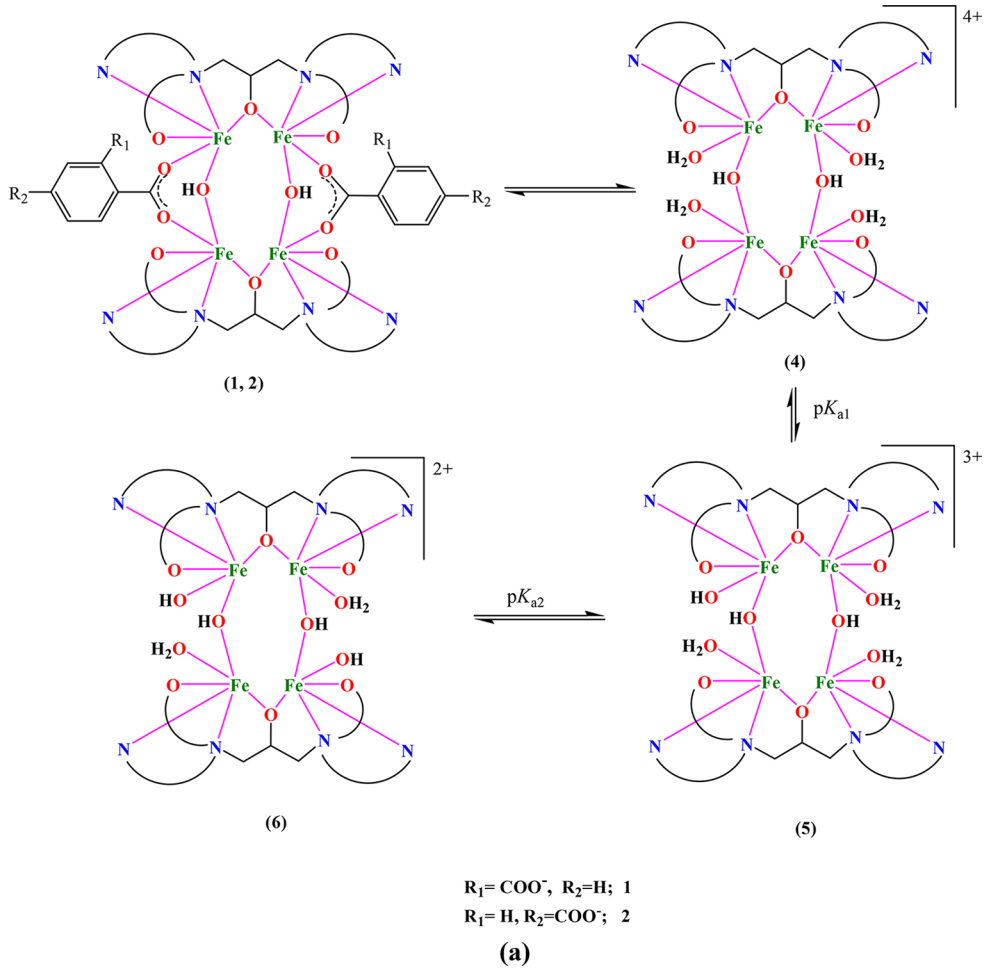

complexes. On the other hand, there are several literature reports on similar iron(III) and zinc(II)-based model complexes[61−63,71−73] that catalyze the phosphoester hydrolysis reactions at substantially high rates with better catalytic

DOI: 10.1021/acs.inorgchem.8b01441
Inorg. Chem. XXXX, XXX, XXX−XXX

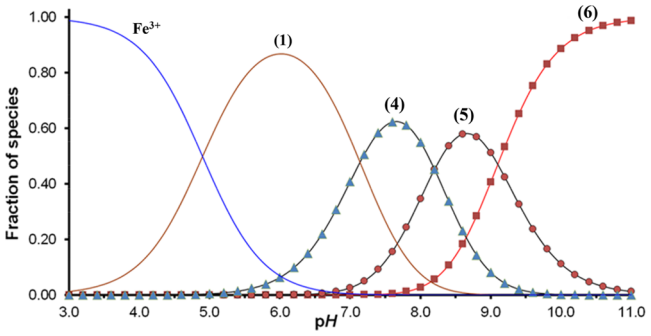

Figure 9. Species distribution diagram for complex **1** as a function of pH.

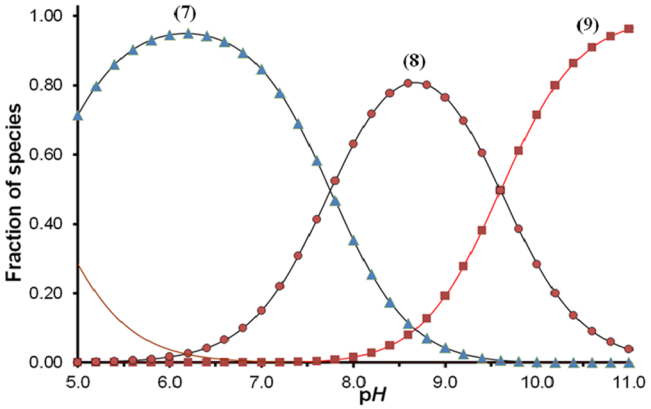

Figure 10. Species distribution diagram for complex **3** as a function of pH.

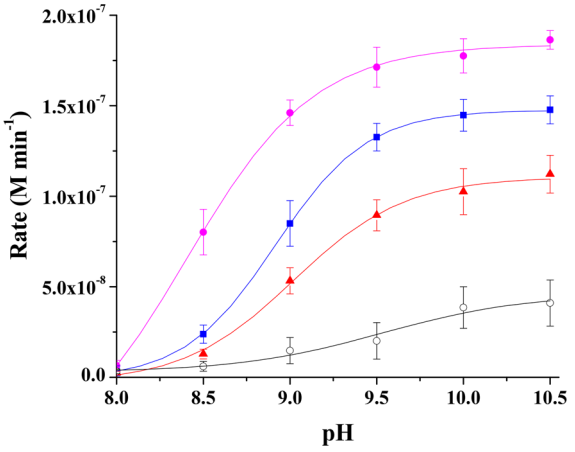

Figure 11. Plot of rate versus pH for the hydrolysis of BNPP in the absence of complex (white circles) and in the presence of complexes **1** (pink circles), **2** (blue squares), and **3** (red triangles). [Complex] = 6.30×10^{-5} M; [BNPP] = 6.25×10^{-3} M; [Buffer] = 20×10^{-3} M; I = 0.1 M ($NaNO_3$) in MeOH-H_2O (1:1; v/v) at 30 °C.

efficiency compared to the present complexes described in this study. In this line, the values of various kinetic parameters for some reported iron(III) and zinc(II)-based model complexes have been summarized in Table 7. The lower catalytic rates for **1**−**3** compared to the literature reports could be most possibly due to the presence of terminally coordinated ligand benzoates that have the tendency to decrease the nucleophilic attack by iron(III)- or zinc(II)-bound hydroxide. Careful literature search reveals that only one of the previous studies reported by Dalle et

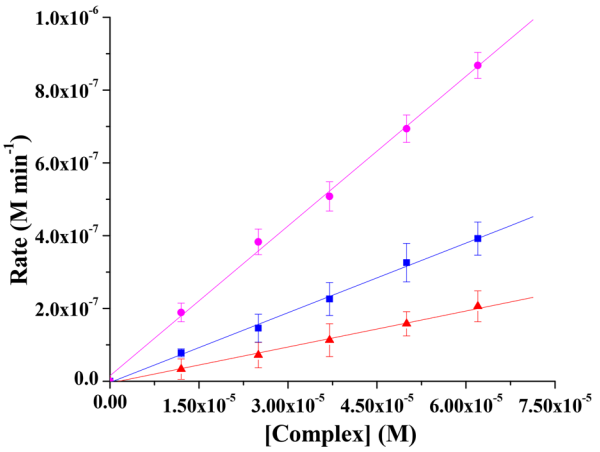

Figure 12. Rate versus complex concentration plot for **1** (pink circles), **2** (blue squares), and **3** (red triangles) for the hydrolysis of BNPP. [BNPP] = 6.25×10^{-3} M; [Buffer] = 20×10^{-3} M; pH ∼ 9.5; I = 0.1 M ($NaNO_3$) in MeOH-H_2O (1:1; v/v) at 30 °C.

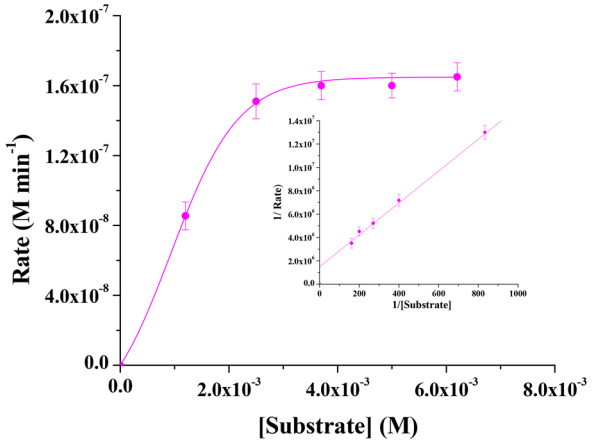

Figure 13. Plot of rate versus concentration of substrate (BNPP) for complex **1**. Inset shows Lineweaver−Burk plot. [Complex] = 6.30×10^{-5} M; [Buffer] = 20×10^{-3} M; pH ∼ 9.5; I = 0.1 M ($NaNO_3$) in MeOH-H_2O (1:1; v/v) at 30 °C.

al.[74] shows zinc(II)-coordinated carboxylates in the complexes during hydrolysis. However, to the best of our knowledge, very few investigations on phosphoester hydrolysis reactions catalyzed by multinuclear iron(III) and zinc(II) complexes in solution are reported in the literature.[75,76]

The potentiometric pH titration results and the corresponding species distribution diagrams reveal that the species that are largely present and stable in solution in the pH range of 9.5−11.0 are $[Fe_4(cpdp)_2(H_2O)_2(OH)_2]^{4+}$ for **1** and **2**, and $[Zn_2(cpdp)(OH)_2]^{-}$ for **3**. Consequently, the possible active species responsible for the catalytic hydrolysis are $[Fe_4(cpdp)_2(H_2O)_2(OH)_2]^{4+}$ for **1** and **2** and $[Zn_2(cpdp)(OH)_2]^{-}$ for **3**. For all three complexes, the metal-bound hydroxide plays a vital role in this catalysis reaction under the specified experimental conditions. Therefore, we have proposed a mechanism for the hydrolysis of BNPP by complexes **1**, **2**, and **3** in Scheme 3. In the proposed mechanism for **1** and **2** (Scheme 3(a)), BNPP preferably binds with one iron(III) ion of an intradinuclear $[Fe^{III}_2]$ subunit in the active species $[Fe_4(cpdp)_2(H_2O)_2(OH)_2]^{4+}$ possessing a labile site that permits the monodentate binding of the substrate to the iron(III) center upon replacement of an iron(III)-bound water

DOI: 10.1021/acs.inorgchem.8b01441
Inorg. Chem. XXXX, XXX, XXX−XXX

Table 6. Kinetic Parameters for Complexes 1, 2, and 3 for the Hydrolysis of BNPP

Complex	k_{cat} (s^{-1})	K_m (M)	V_{max} (M s^{1-})	k_{cat}/K_m (M^{-1} s^{-1})	k_{cat}/k_{uncat}
1	$(2.73 \pm 0.13) \times 10^{-5}$	$(4.80 \pm 0.24) \times 10^{-3}$	$(6.83 \pm 0.34) \times 10^{-9}$	$(5.68 \pm 0.28) \times 10^{-3}$	$(2.93 \pm 0.14) \times 10^{2}$
2	$(1.06 \pm 0.07) \times 10^{-5}$	$(4.08 \pm 0.29) \times 10^{-3}$	$(2.66 \pm 0.18) \times 10^{-9}$	$(2.59 \pm 0.18) \times 10^{-3}$	$(1.13 \pm 0.07) \times 10^{2}$
3	$(3.05 \pm 0.18) \times 10^{-6}$	$(7.60 \pm 0.46) \times 10^{-3}$	$(7.64 \pm 0.34) \times 10^{-10}$	$(4.02 \pm 0.20) \times 10^{-4}$	$(3.28 \pm 0.15) \times 10^{1}$

Table 7. pK_a's and Kinetic Parameters of Reported Di- and Tetranuclear Iron and Zinc Model Complexes for Phosphoester Hydrolysis

Complex	Substrate	pK_{a1}	pK_{a2}	k_{cat} (s^{-1})	K_M (mM)	k_{cat}/K_M (s^{-1} M^{-1})	ref
$[Fe^{II}_2LCl_3]\cdot 3H_2O$	BNPP	5.3	8.5	$(5.1 \pm 0.2) \times 10^{-5}$	$(3.1 \pm 0.2) \times 10^{-3}$	$(1.7 \pm 0.1) \times 10^{-2}$	60
$[Fe^{III}_2(L^3)(OH)(OH_2)_2]^{4+}$	BDNPP	5.3 ± 0.03	9.3 ± 0.10	$(6.48 \pm 0.34) \times 10^{-4}$	(7.38 ± 0.69)	$(8.79 \pm 0.12) \times 10^{-2}$	67
$[Fe^{II}_2(H_2L^4)(OAc)_2]^{+}$	BDNPP			$(2.37 \pm 0.29) \times 10^{-3}$	3.53 ± 0.68	0.67	71
$\{[(Fe_2^{III}(\mu\text{-OAc}))]L\}^{+}$	BDNPP	6.7	8.70	2.94×10^{-3}	0.78	3.72×10^{-4}	72
$[Fe^{III}_4(HPBA)_2(\mu\text{-OAc})_2(\mu\text{-O})(\mu\text{-OH})(OH_2)_2]^{2+}$	BDNPP	5.4	8.4	$(1.6 \pm 0.2) \times 10^{-3}$	7.4 ± 0.6	2.16×10^{-4}	61
$[Fe^{III}Zn^{II}(L\text{-}CH_3)(\mu OH)(H_2O)]^{+2}$	BDNPP	4.8	8.4	9.20×10^{-4}	(3.05 ± 0.10)	2.16×10^{-2}	73
$[Fe^{III}Zn^{II}L^2]$	BDNPP	5.9 ± 0.05	7.7 ± 0.09	$(32.1 \pm 3.31) \times 10^{-5}$	(34.0 ± 5.70)	0.09	68
$[Zn^{II}_2(L_{-2H})(AcO)(H_2O)][Zn^{II}_2L']$	BNPP	7.2	8.1	4.6×10^{-6}	6.15×10^{-2}	4.49×10^{-5}	69
$[Zn^{II}_2(HL^1)(CH_3COO)]^{+}$	BNPP			$(1.26 \pm 0.06) \times 10^{-6}$	$(1.96 \pm 0.25) \times 10^{-3}$	0.64×10^{-3}	70
$[Zn^{II}_2(H_2L^2)(OAc)_2]^{+}$	BDNPP	7.7	9.5	$(3.20 \pm 0.21) \times 10^{-3}$	(9 ± 1)	0.34×10^{-3}	62
$[Zn^{II}_4(TPPNOL)_2(OAc)_3]^{3+}$	BDNPP	7.7	9.5	1.28×10^{-4}	4.4 ± 1	2.90×10^{-3}	63

molecule. Next, an intramolecular nucleophilic attack by the iron(III)-bound hydroxide of the same intradinuclear $[Fe^{III}_2]$ subunit to the phosphorus atom leads to the formation of free phosphate and *p*-nitrophenolate in solution. It is worth mentioning that the direct coordination of BNPP to the iron(III) ion activates the P−O bond for the nucleophilic attack. This hypothesis is strongly supported by DFT calculations which indicate that the substrate BNPP does not interact through bridging binding, instead it interacts through monodentate binding. Preliminary DFT calculations reveal that the energies ($\Delta G^{\ddagger}$) for monodentate (TSA) and bridging (TSB) binding of the substrate with an intradinuclear $[Fe^{III}_2]$ subunit are calculated to be −6065.01 au and −6064.41 au (Figures 14(A) and 14(B)), respectively. The different energy values for monodentate and bridging binding indicate that the dinuclear $[Fe^{III}_2]$ subunit undergoes different degrees of structural reorganization during forming the respective transition states. The relatively lower energy value for TSA by −0.60 au (−1569.52 kJ/mol) confirms a preference for monodentate binding of the substrate. On the other hand, in the proposed mechanism for **3** (Scheme 3(b)), the first step involves the activation of BNPP by complex **3** that happens via the bridging coordination of phosphate which has also been strongly supported by DFT calculations. Then in the second step, the deprotonation of solvent water molecule occurs by a zinc(II)-bound hydroxide which acts as a general base-catalyst, followed by the nucleophilic attack of this free hydroxide to the phosphorus atom of the substrate. In fact, this would require the concerted action of the Lewis acid activation and the intramolecular general base catalysis by a zinc(II)-bound hydroxide ion. As can be seen, the DFT calculations show that the energies ($\Delta G^{\ddagger}$) for monodentate (TSA′) and bridging (TSB′) binding of the substrate with an intradinuclear $[Zn^{II}_2]$ subunit are evaluated to be −7096.35 au and −7098.05 au (Figures 14(C) and 14(D)), respectively. The significantly higher energy value for TSA′ indicates that its formation is unfavorable during hydrolysis reaction. Therefore, the substrate interacts with an intradinuclear $[Zn^{II}_2]$ subunit of **3** via the bridging coordination of phosphate. Generally, if the substrate binds monodentately to one metal ion, a terminally bound hydroxide or second coordination sphere hydroxide is the more likely candidate to act as a nucleophile.[30] Again, if the substrate binds to two metal ions in the μ-1,3 bidentate bridging coordination mode, the metal ion bridging hydroxide or an outer sphere water molecule that may be activated becomes the nucleophile.[30] In this regard, Gahan and co-workers have studied the role of zinc coordinated deprotonated alcohol and hydroxide as potential nucleophilic species in the reactions of dinuclear phosphatase mimetics.[77] However, an unambiguous identification of the appropriate nucleophile in phosphoester hydrolysis reactions is quite difficult.[69,78,79]

We have compared the phosphatase-like activity of complexes **1**, **2**, and **3** by rationalizing their k_{cat} values and found that the order of catalytic activity is given as **1** > **2** > **3**. As expected, for any complex to act as an competent catalyst for substrate hydrolysis, first the arriving substrate should be bounded effectively to the catalyst, which is generally controlled by the geometrical and electronic factors of the metal−ligand interactions. In the present study, the different catalytic activities of complexes **1** and **2** to hydrolyze BNPP could be most possibly due to the difference in effective concentrations of the active tetrairon(III) species $[Fe_4(cpdp)_2(H_2O)_2(OH)_2]^{4+}$ in solution at pH ∼ 9.5, as shown by the species distribution curves. The higher catalytic activity of **1** compared to that of **2** could be attributed to the higher effective concentration of the active species of **1** than that of **2** in solution. Again, the significantly lower catalytic activity of **3** compared to that of **1** and **2** toward BNPP hydrolysis is most likely due to the following reasons. First, there are zinc(II) ions present in complex **3** instead of iron(III) ions. Second, the coordination geometry around the metal centers in **3** is different compared to that in **1** and **2**. The octahedral coordination geometry around the iron(III) centers with loosely bound aqua ligand in the active species of **1** and **2** facilitates the formation of the complex-substrate intermediates during the interaction with BNPP compared to that in the case of the trigonal bipyramidal geometry around the zinc(II) centers in the active species of **3**. Third, the effective concentration of the active species of **3** is lower than that of **1** and **2**, in solution. Finally, during hydrolysis, whereas the activation of substrate by complexes **1** and **2** occurs via the monodentate coordination of

DOI: 10.1021/acs.inorgchem.8b01441
Inorg. Chem. XXXX, XXX, XXX−XXX

Scheme 3. Proposed Mechanism for the Hydrolysis of BNPP by the Complexes (a) 1 and 2 (half part of each complex is shown for clarity) and (b) 3

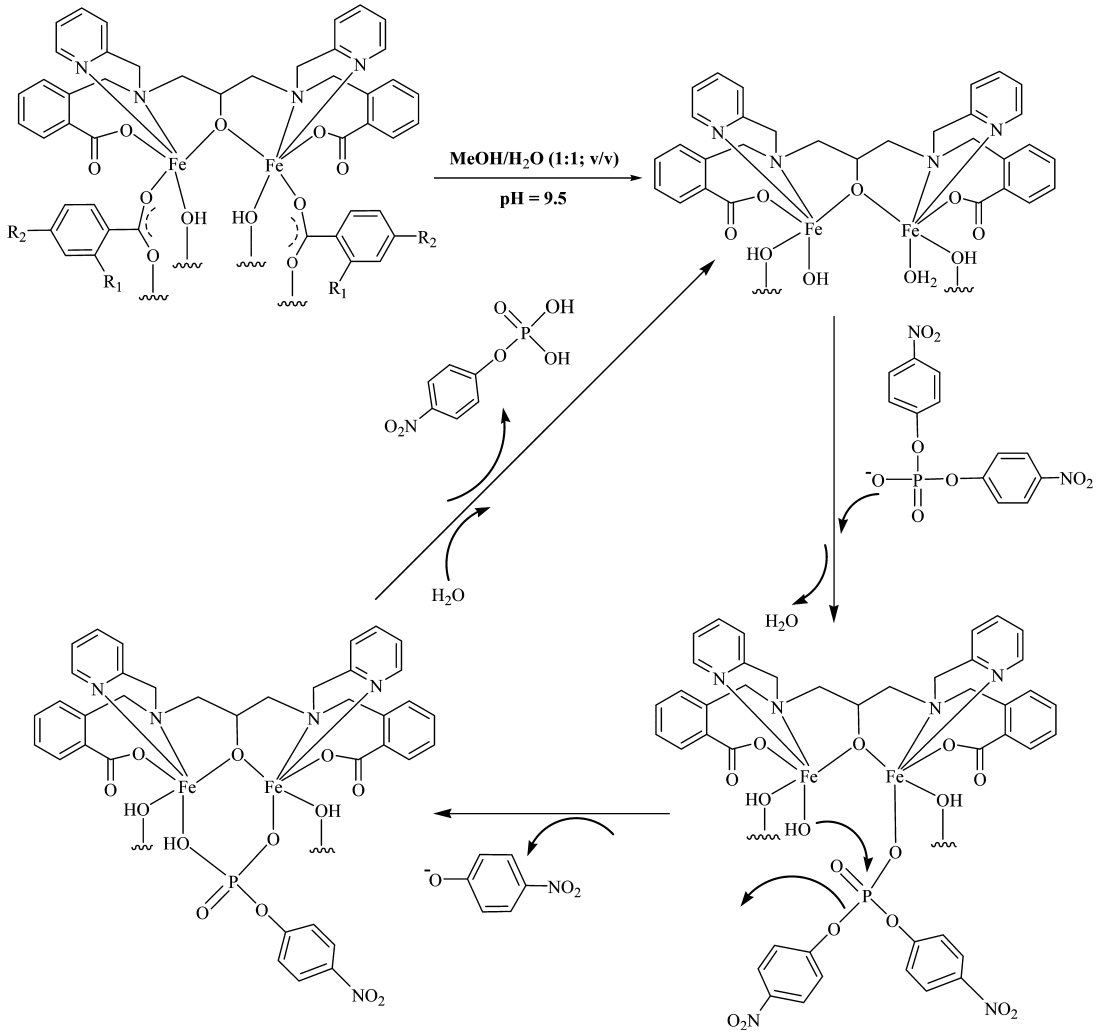

(a)

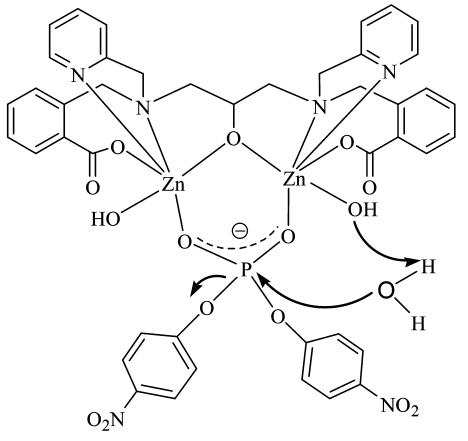

(b)

phosphate of BNPP, the activation of substrate by complex **3** happens via the bridging coordination of phosphate which has been further supported by DFT calculation.

To examine the effect of phthalate, terephthalte, and succinate ions on the rate of hydrolysis of BNPP by complexes **1**−**3**, the hydrolysis reaction was performed as a function of their concentration. The representative Figures S21 and S22 of the Supporting Information indicate the percentage of inhibition on the hydrolysis with increasing concentrations of exogeneous dicarboxylates such as phthalate and succinate ions which significantly inhibit the hydrolysis reaction. When the individual phthalate, terephthalte, and succinate ion concentration equals

DOI: 10.1021/acs.inorgchem.8b01441
Inorg. Chem. XXXX, XXX, XXX−XXX

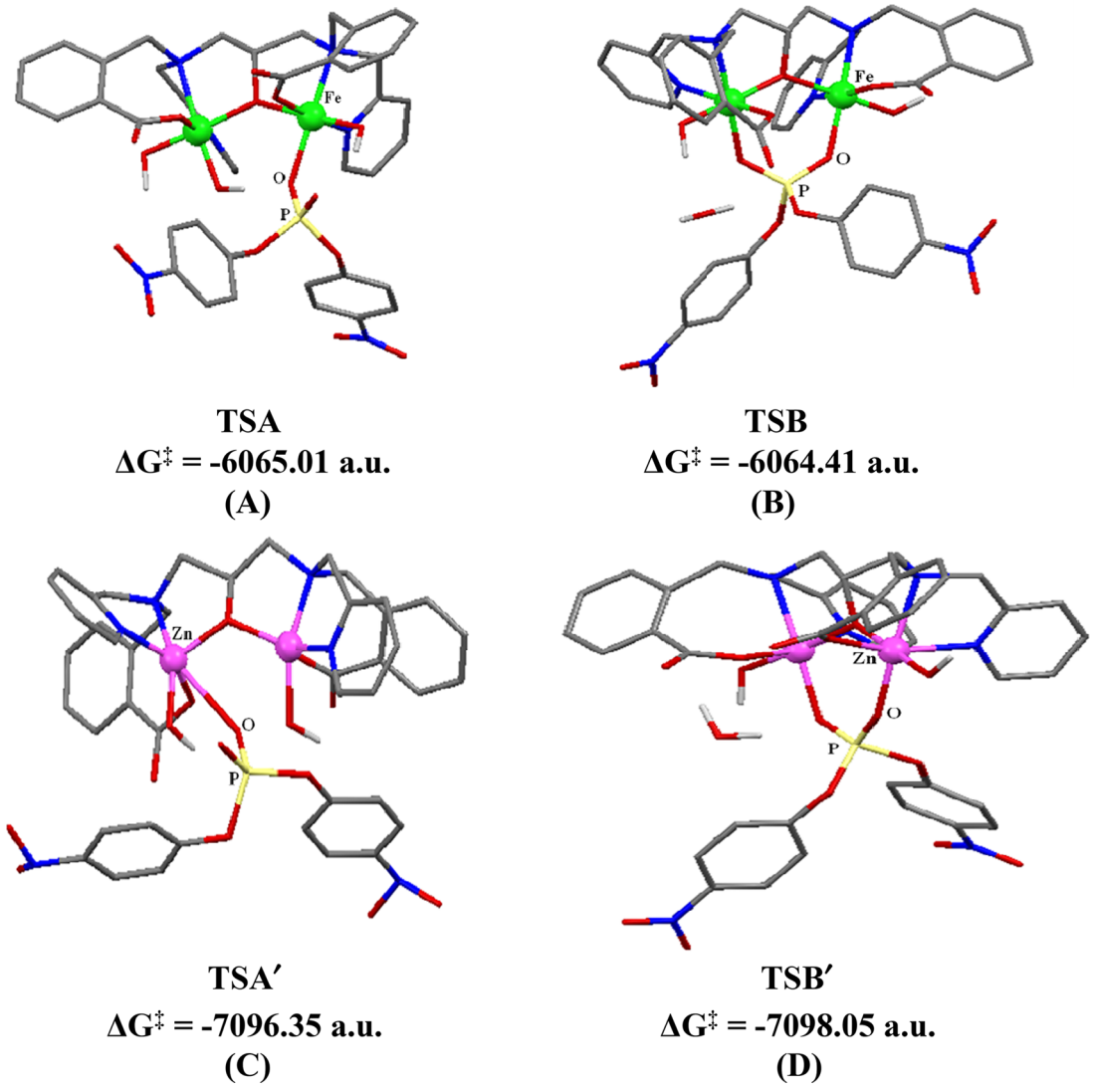

Figure 14. Calculated structures and energies for monodentate and bridging binding of BNPP; (A) monodentate and (B) bridging binding of BNPP with an intradinuclear $[Fe^{III}_2]$ subunit of **1** and **2**; (C) monodentate and (D) bridging binding of BNPP with an intradinuclear $[Zn^{II}_2]$ subunit of **3**.

the BNPP concentration, a reduction of the rate by 48%, 55%, and 50% is observed for **1**, **2**, and **3**, respectively. From these results it is clearly evident that phthalate, terephthalte, and succinate ions are released from **1**, **2**, and **3**, respectively, to yield their corresponding active species during hydrolysis experiments.

CONCLUSION

In conclusion, we have successfully prepared and characterized phthalate, terephthalate, and succinate incorporated, three new tetranuclear complexes of iron(III) and zinc(II) by utilizing a carboxylate- and pyridine-based polydentate ligand. Structural analyses reveal that complexes **1** and **2** are the bis(μ-phthalato/μ-hydroxo)- or bis(μ-terephthalato/μ-hydroxo)-bridged dimers of dimers and complex **3** is a μ_4-succinate-bridged dimer of dimers. Accordingly, the dicarboxylates, such as phthalate, terephthalate, and succinate, bridge two dinuclear $[Fe_2(cpdp)]^{3+}$ or $[Zn_2(Hcpdp)]^{2+}$ units to yield tetranuclear complexes, showing that the flexibility of the carboxylate backbone plays an important role in the shape of the molecular polyhedra. In addition to the bis(μ-phthalato/μ-hydroxo), bis(μ-terephthalato/μ-hydroxo), or μ_4-succinate bridges, the occurrence of hydrogen bonding interactions and moderate intramolecular $\pi\cdots\pi$ stacking interactions appears to provide the stabilizing factors to the Fe_4 and Zn_4 crystal lattices. It is worth mentioning that four iron centers in the tetranuclear unit are located at the corners of a rectangle/quadrilateral feature forming a concave shaped octagonal core in **1** and **2**. It is also interesting that the succinate ligand in complex **3** exhibits a $\mu_4{:}\eta^1{:}\eta^1{:}\eta^1{:}\eta^1$ bridging coordination mode connecting four zinc centers. Our investigation into the phosphatse-like activity shows that all three complexes are capable of cleaving the phosphoester bond in bis(*p*-nitrophenyl) phosphate (BNPP) with an average acceleration of hydrolysis up to 1.46×10^2 fold at pH ~ 9.5 over the background reaction. All three complexes are found to reveal comparable pK_a values of the coordinated water molecules indicating the metal ion bound hydroxide or an outer sphere water molecule that may be activated acts as the nucleophile. In an attempt to support the proposed mechanistic pathways for the present systems, computational methods have been performed. DFT calculations show that, for **1** and **2**, the substrate preferably binds with one iron(III) ion of an intradinuclear $[Fe^{III}_2]$ subunit containing a labile site that allows the monodentate binding of the substrate to the iron(III) center.

DOI: 10.1021/acs.inorgchem.8b01441
Inorg. Chem. XXXX, XXX, XXX−XXX

On the other hand, DFT calculations suggest that the substrate binds with two zinc(II) ions of an intradinuclear $[Zn^{II}_2]$ complex of **3** through bridging coordination of the phosphate group. The comparison of turnover rates indicates that complexes **1** and **2** are better catalysts among the three complexes toward the hydrolysis of BNPP in alkaline aqueous-methanol solution.

EXPERIMENTAL SECTION

Synthesis of *N,N′*-Bis[2-carboxybenzomethyl]-*N,N′*-bis[2-pyridylmethyl]-1,3-diaminopropan-2-ol, H_3cpdp. The ligand H_3cpdp was synthesized according to our previously published procedure.[39] The composition of the ligand was established as H_3cpdp·LiCl·3LiBr·14H_2O by elemental and thermogravimetric analyses. Yield: 4.018 g (77%). Anal. Calcd. for $C_{31}H_{32}N_4O_5$·LiCl·3LiBr·14H_2O: C, 33.98%; H, 5.51%; N, 5.11%; Cl, 3.24%; Br, 21.88%. Found: C, 33.88%; H, 5.54%; N, 5.27%; Cl, 2.91%; Br, 21.49%. FTIR (cm^{-1}): ν = 3389(b), 2084(b), 1634(s), 1567(vs), 1441(s), 1399(s), 1298(s), 1154(s), 1094(s), 972(s), 761(s). ^{1}H NMR (400 MHz, D_2O, room temperature, δ): 8.47 (d, 2H), 7.81 (t, 2H), 7.64 (d, 2H), 7.39–7.51 (m, 8H), 7.27 (d, 2H), 4.47 (d, 8H), 4.01–4.20 (m, 1H), 3.38 (d, 2H), 3.13 (t, 2H). ^{13}C NMR (100 MHz, D_2O, room temperature, δ): 174.65, 149.32, 148.91, 143.99, 141.31, 138.87, 137.23, 133.20, 130.88, 130.44, 125.01, 124.68, 60.47, 60.25, 57.50, 57.11. Mass spectrum (ESI): m/z 565 (100%) (M^+ = {H_3cpdp·H_2O+Li}$^+$), 559 (81%) (M^+ = {H_3cpdp·H_2O+H}$^+$). TGA analysis: loss of H_2O {136 °C - 273 °C: 23.00% (Calcd.); 23.35% (Found)}; loss of CO_2 {290 °C − 367 °C: 8.03% (Calcd.); 8.39% (Found).

*Synthesis of [Fe_4(cpdp)$_2$(phth)$_2$(OH)$_2$]·8H_2O (**1**).* A solution of $FeCl_3$ (0.150 g, 0.92 mmol) in methanol (10 mL) was added to a solution of H_3cpdp (0.511 g, 0.46 mmol) and $NaHCO_3$ (0.116 g, 1.38 mmol) in methanol (10 mL). The reaction mixture was stirred for 1 h resulting in a brown solution. Then, to this brown solution, phthalic acid (0.076 g, 0.46 mmol) in water (5 mL) was slowly added and the stirring was continued for another 2 h. Finally, the solution became greenish brown and it was filtered to remove any insoluble precipitate. Slow diethyl ether diffusion into the clear filtrate diluted by 5 mL acetonitrile produced brown plate-shaped single crystals suitable for X-ray diffraction after 5–7 days. Yield: 0.275 g (65%). Anal. Calcd. for $C_{78}H_{84}N_8O_{28}Fe_4$: C, 51.90%; H, 4.69%; N, 6.21%; Fe, 12.38%. Found: C, 51.78%; H, 4.61%; N, 6.32%; Fe, 12.51%. FTIR (cm^{-1}): ν = 3397(b), 1722(s), 1607(s), 1599(s), 1574(s), 1531(s) 1488(s), 1449(s), 1411(s), 1360(s), 1249(s), 1152(s), 1024(s), 981(s), 870(s), 760(s), 727(s), 671(s). UV–vis (MeOH/H_2O): λ_{max} (ε, $M^{-1}cm^{-1}$) = 508 (590), 452 (2180), 261 (10900), 228 (14030), 206 (33660). Magnetic moment, μ_{eff} (tot.): 11.62 μ_B; μ_{eff}/Fe: 5.81 μ_B. Mass spectrum (ESI): m/z 1661 (77%) (M^+ = {[Fe_4(cpdp)$_2$(phth)$_2$(OH)$_2$]+H}$^+$), 739 (100%) (M^+ = [Fe_4(cpdp)$_2$(OH)$_4$(CH_3OH)$_3$(H_2O)]$^{2+}$), 665 (83%) (M^+ = [Fe_4(cpdp)$_2$(O_2)]$^{2+}$).

*Synthesis of [Fe_4(cpdp)$_2$(terephth)$_2$(OH)$_2$] (**2**).* This compound was prepared as microcrystalline powder by carrying out reaction of H_3cpdp with $FeCl_3$, $NaHCO_3$, and terephthalic acid following the above procedure. Yield: 0.295 g (76%). Anal. Calcd. for $C_{78}H_{68}N_8O_{20}Fe_4$: C, 56.41%; H, 4.13%; N, 6.75%; Fe, 13.45%. Found: C, 56.59%; H, 4.24%; N, 6.69%; Fe, 13.29%. FTIR (KBr, cm^{-1}): ν = 3445(b), 1631(s), 1610(s), 1585(s), 1566(s), 1527(s), 1449(s), 1385(s), 1242(s), 1187(s), 1061(s), 1051(s), 872(s), 772(s), 616(s). UV–vis (MeOH/H_2O): λ_{max} (ε, $M^{-1}cm^{-1}$) = 504 (930), 449 (3910), 262 (7430), 238 (11800), 203 (34510). Magnetic moment, μ_{eff} (tot.): 11.78 μ_B; μ_{eff}/Fe: 5.89 μ_B. Mass spectrum (ESI): m/z 1661 (8%) (M^+ = {[Fe_4(cpdp)$_2$(terephth)$_2$(OH)$_2$]+H}$^+$), 665 (100%) (M^+ = [Fe_4(cpdp)$_2$(O_2)]$^{2+}$).

*Synthesis of [Zn_4(Hcpdp)$_2$(suc)]Br_2·12H_2O (**3**).* A solution of $ZnCl_2$ (0.125 g, 0.92 mmol) in methanol (10 mL) was added to a solution of H_3cpdp (0.511 g, 0.46 mmol) and NaOH (0.055g, 1.38 mmol) in methanol (10 mL). The reaction mixture was stirred for 1 h resulting in a light yellow solution. Then, an aqueous solution (5 mL) of sodium succinate (0.124 g, 0.46 mmol) was added to this solution and the stirring was continued for another 1 h. To remove any insoluble precipitate, the solution was filtered. Light yellow needle-shaped single crystals suitable for X-ray diffraction study were obtained after 7–10 days by slow diethyl ether diffusion into the clear filtrate. Yield: 0.321 g (73%). Anal. Calcd. for $C_{66}H_{88}N_8O_{26}Br_2Zn_4$: C, 43.30%; H, 4.84%; N, 6.12%; Zn, 14.29%. Found: C, 43.23%; H, 4.63%; N, 6.29%; Zn, 14.51%. FTIR (cm^{-1}): ν = 3415(b), 1609(s), 1583(s), 1562(s), 1486(s), 1437(s), 1376(s), 1307(s), 1157(s), 1124(s), 1054(s), 1029(s), 988(s), 913(s), 866(s), 764(s), 721(s), 685(s). ^{1}H NMR (400 MHz, DMSO-d_6, room temperature): δ (ppm) = 2.81 (t, 4H, succinate), 3.23–4.12 (m, 26H, aliphatic), 6.85–7.56 (m, 32H, aromatic). ^{13}C NMR (100 MHz, DMSO-d_6, room temperature): δ (ppm) = 34.47 (2C, CH_2, succinate), 54.83 (2C, CH_2, aliphatic), 61.67 (2C, CH_2, aliphatic), 62.22 (2C, CH_2, aliphatic), 63.80 (1C, CH, aliphatic), 122.34 (2C, CH, aromatic), 123.32 (2C, CH, aromatic), 128.20 (2C, CH, aromatic), 128.97 (2C, CH, aromatic), 129.81 (2C, CH, aromatic), 131.25 (2C, CH, aromatic), 131.82 (2C, CH, aromatic), 138.87 (2C, CH, aromatic), 139.95 (2C, CH, aromatic), 146.46 (2C, CH, aromatic), 156.88 (2C, CH, aromatic), 176.88 (2C, bidentate bridging carboxylate, succinate), 181.68 (2C, monodentate terminal carboxylate, aromatic). UV–vis (MeOH/H_2O): λ_{max} (ε, $M^{-1}cm^{-1}$) = 260 (20340), 228 (22550). Mass spectrum (ESI): m/z 1483 (4%) (M^+ = {[Zn_4(cpdp)$_2$(suc)(H_2O)$_2$]+H}$^+$), 811 (100%) (M^+ = [Zn_2(cpdp)(H_2O)(CH_3OH)$_4$]$^+$), 751 (60%) (M^+ = [Zn_2(cpdp)-(H_2O)$_3$(CH_3OH)]$^+$).

Reagents and Solvents. 2-Carboxybenzaldehyde, 2-picolylchloride hydrochloride, 1,3-diamino-2-propanol and lithium hydroxide were purchased from Sigma-Aldrich Chemie GmbH, Germany. Ferric chloride, zinc chloride, sodium succinate, phthalic acid, terephthalic acid, sodium hydroxide, sodium bicarbonate, and sodium borohydride were purchased from Merck, India. CAPS buffer was purchased from SRL, India. All other chemicals and solvents were reagent grade materials and were used as received without further purification.

Instrumentation and Physical Measurements. Microanalyses (C,H,N) were performed with a PerkinElmer 2400 CHNS/O Series II elemental analyzer. The chloride and bromide contents in the ligand H_3cpdp were measured by potentiometric titration using $AgNO_3$ in aqueous solution with a Mettler Toledo Seven Compact S220 digital Ion/pH meter.[39] Quantitative analysis of iron content in complexes **1** and **2** was carried out by volumetric titration in aqueous-acidic medium using $K_2Cr_2O_7$ solution. The zinc content in complex **3** was measured by carrying out complexometric titration in aqueous medium using Na_2H_2EDTA solution. FTIR spectra were recorded on a PerkinElmer L120–000A spectrometer using KBr pellet in the range of 450–4000 cm^{-1}. UV–vis spectra were run on a Shimadzu UV 1800 (200–900 nm) (1 cm quartz cell) spectrophotometer. ^{1}H and ^{13}C NMR spectra were obtained on a Bruker AC 400 NMR spectrometer. Mass spectrometric experiments of the ligand and complexes were performed using a Micromass Q-Tof Micro (Waters) mass spectrometer. The room temperature magnetic susceptibilities were measured by using a home-built Gouy balance fitted with a polytronic DC power supply. Diamagnetic corrections for ligand susceptibilities were made using Pascal's constant. Variable temperature magnetic susceptibility of powdered microcrystalline sample was measured between 2 and 300 K with a SQUID magnetometer (MPMS-7, Quantum Design) in an external magnetic field of 1 T. Thermogravimetric analysis of the ligand was completed by a NETZSCH STA 449F3 thermal analyzer.

Potentiometric pH Titrations. The potentiometric pH titrations of the complexes were performed by a Mettler Toledo Seven Compact S220 digital Ion/pH meter in MeOH-H_2O (1:1; v/v) solution with I = 0.1 M of $NaNO_3$ at 30 °C. A correction of pH value of ∼0.051 units were deducted from the measured pH readings to balance the normal liquid junction potential of the methanol–water solvent mixture.[80] Applying the HYPERQUAD 2000 and HySS programs, all computations and species distribution diagrams were completed.[81] A typical pH-metric titration was conducted by titrating 1 mM MeOH–H_2O (1:1; v/v) solution of each complex with 0.01 M solution of NaOH. Using these pH-metric titration data, the pK_a values of the coordinated water molecules in **1**, **2**, and **3** in solution were evaluated.

Phosphatase-like Activity and Kinetic Measurements. Complexes **1**, **2**, and **3** were examined for phosphatase-like activity through

DOI: 10.1021/acs.inorgchem.8b01441
Inorg. Chem. XXXX, XXX, XXX–XXX

the hydrolysis of model substrate, bis(*p*-nitrophenyl) phosphate (BNPP) under pseudo-first-order reaction conditions. We have run the kinetic experiments in 3 mL UV cells in MeOH-H_2O (1:1; v/v) solution in 20 mM CAPS buffer (pH ∼ 9.5). The ionic strength was adjusted to I = 0.1 M $NaNO_3$. A requisite amount of 1 mM stock solution of each complex was added separately to maintain the concentration of each complex at 0.06 mM in the cuvette, and a requisite amount of 50 mM BNPP stock solution was added to vary the concentrations from 1.25 mM to 6.25 mM in the cuvette. To complete the final volume in the cuvette, a requisite amount of buffer solution was added. Using a thermostatic cell (30 °C), all the ingredients were mixed properly, and the spectra were recorded at 400 nm, where the molar extinction coefficient for the hydrolysis product *p*-nitrophenolate is 18500 M^{-1} cm^{-1}.[82] The total amount of *p*-nitrophenol/phenolate was calculated by means of its pK_a (7.15).[82] All the measurements were performed in triplicate, and the average values with standard deviations were accepted.

X-ray Crystallography and Data Analysis. X-ray crystal data for **1** were collected at 293 K using a diffractometer with SuperNova, Dual, Cu at zero, EOS area detector using graphite monochromated Mo Kα radiation (λ = 0.71073 Å). Similarly, X-ray crystal data for **3** were recorded at 100 K on a diffractometer with SuperNova, Dual, Cu at zero, Eos area detector, and graphite-monochromated Cu Kα radiation (λ = 1.54184 Å). The statistical tests were used to determine the monoclinic space group $C2/c$ for **1** and orthorhombic space group *pnna* for **3**. A total of 9972 data were obtained for complex **1** with Miller indices h_{min} = −43, h_{max} = 29, k_{min} = −6, k_{max} = 18, l_{min} = −24, and l_{max} = 19, in the range of 1.856 < θ < 28.611° using ω oscillation frames. Similarly, a total of 5500 data were recorded for complex **3** with Miller indices h_{min} = −26, h_{max} = 26, k_{min} = −22, k_{max} = 17, l_{min} = −22, and l_{max} = 21, in the range of 4.592 < θ < 66.059° using ω oscillation frames. Employing the multiscan method,[83] absorption correction of the data was achieved giving minimum and maximum transmission factors. Both the two structures were solved by direct methods using the program SIR-97[84] and refined by full-matrix least-squares methods on $F2$ with SHELX[85,86] and Olex2.[87] While part of one phthalate group was modeled over two positions, the Fe^{3+}, $cpdp^{3-}$ ligand, and other phthalate were not. These disorders over two positions affect the quality of the single crystal X-ray data and the refining model of structure **1**. The difference Fourier map was used to locate the hydrogen atoms. Hydrogen atoms of the complexes were included in idealized positions (C−H, 0.96 Å) and refined as riding models. Hydrogen atoms of the solvent water molecules of **1** cannot be located precisely and were omitted.

Theoretical Calculation. Theoretical calculation[88] concerning the structure optimization of complexes **1**, **2**, and **3** was carried out using the B3LYP method[89−91] and 6-311G basis set.[92,93] In order to substantiate the proposed mechanism, DFT calculation (structure optimization and energy calculation) was also performed on the transition states using the same method and basis set.

■ ASSOCIATED CONTENT

Supporting Information

The Supporting Information is available free of charge on the ACS Publications website at DOI: 10.1021/acs.inorgchem.8b01441.

Temperature dependence of χ_MT for **1**; FT-IR, UV−vis, and ESI-mass spectra of **1**, **2**, and **3**; Packing diagram of **3**; Views of DFT optimized structures and intramolecular $\pi\cdots\pi$ stacking interactions of **1** and **3**; Potentiometric titration curves and rate versus substrate concentration plots for **2** and **3**; Species distribution diagram of **3**; Plots of percentage inhibition of BNPP for **1** and **3**; Table for characteristic FTIR absorptions of the complexes (PDF)

Accession Codes

CCDC 1823467−1823468 contain the supplementary crystallographic data for this paper. These data can be obtained free of charge via www.ccdc.cam.ac.uk/data_request/cif, or by emailing data_request@ccdc.cam.ac.uk, or by contacting The Cambridge Crystallographic Data Centre, 12 Union Road, Cambridge CB2 1EZ, UK; fax: +44 1223 336033.

■ AUTHOR INFORMATION

Corresponding Author

*E-mail: mbera2009@klyuniv.ac.in; Fax: +91 33 25828282; Tel: +91 33 25828282 x306.

ORCID

Gonela Vijaykumar: 0000-0002-1249-7347

Manindranath Bera: 0000-0001-6230-5756

Notes

The authors declare no competing financial interest.

■ ACKNOWLEDGMENTS

The work was strongly supported by The Council of Scientific & Industrial Research (CSIR) (Grant No.: 01(2732)/13/EMR-II), New Delhi. The DST-FIST and UGC-SAP programs are acknowledged for providing the instrumental facilities in the Department of Chemistry, University of Kalyani. The Contingency Grant provided by the DST-PURSE program in the Department of Chemistry is also acknowledged. The authors are indebted to Dr. Subhajit Bandyopadhyay, IISER-Kolkata for plotting the species distribution diagrams. S.H. greatly acknowledges the RGNF received from UGC, New Delhi. N.D. thanks the University of Kalyani for providing a University Research Fellowship.

■ REFERENCES

(1) Dempsey, J. L.; Esswein, A. J.; Manke, D. R.; Rosenthal, J.; Soper, J. D.; Nocera, D. G. Molecular Chemistry of Consequence to Renewable Energy. *Inorg. Chem.* **2005**, *44*, 6879−6892.

(2) Holm, R. H.; Kennepohl, P.; Solomon, E. I. Structural and Functional Aspects of Metal Sites in Biology. *Chem. Rev.* **1996**, *96*, 2239−2314.

(3) Dance, I. Nitrogenase: A General Hydrogenator of Small Molecules. *Chem. Commun.* **2013**, *49*, 10893−10907.

(4) Kaila, V. R. I.; Verkhovsky, M. I.; Wikström, M. Proton-Coupled Electron Transfer in Cytochrome Oxidase. *Chem. Rev.* **2010**, *110*, 7062−7081.

(5) Friedle, S.; Reisner, E.; Lippard, S. J. Current Challenges of Modeling Diiron Enzyme Active Sites for Dioxygen Activation by Biomimetic Synthetic Complexes. *Chem. Soc. Rev.* **2010**, *39*, 2768−2779.

(6) Dau, H.; Limberg, C.; Reier, T.; Risch, M.; Roggan, S.; Strasser, P. The Mechanism of Water Oxidation: From Electrolysis via Homogeneous to Biological Catalysis. *ChemCatChem* **2010**, *2*, 724−761.

(7) Gloaguen, F.; Rauchfuss, T. B. Small Molecule Mimics of Hydrogenases: Hydrides and Redox. *Chem. Soc. Rev.* **2009**, *38*, 100−108.

(8) Kurtz, J. D. M. Oxo and Hydroxo-Bridged Diiron Complexes: A Chemical Perspective on a Biological Unit. *Chem. Rev.* **1990**, *90*, 585−606.

(9) Feig, A. L.; Lippard, S. J. Reactions of Non-Heme Iron(II) Centers with Dioxygen in Biology and Chemistry. *Chem. Rev.* **1994**, *94*, 759−805.

(10) Vincent, J. B.; Olivier-Lilley, G. L.; Averill, B. A. Proteins Containing Oxo-Bridged Dinuclear Iron Centers: A Bioinorganic Perspective. *Chem. Rev.* **1990**, *90*, 1447−1467.

(11) Holm, R. H.; Lo, W. Structural Conversions of Synthetic and Protein-Bound Iron-Sulfur Clusters. *Chem. Rev.* **2016**, *116*, 13685−13713.

DOI: 10.1021/acs.inorgchem.8b01441
Inorg. Chem. XXXX, XXX, XXX−XXX

(12) Pathak, C.; Gupta, S. K.; Gangwar, M. K.; Prakashan, A. P.; Ghosh, P. Modelling the Active Site of the Purple Acid Phosphatase Enzyme with Hetero-Dinuclear Mixed Valence M(II)-Fe(III) [M = Zn, Ni, Co, and Cu] Complexes Supported over a [N_6O] Unsymmetrical Ligand. *ACS Omega* **2017**, *2*, 4737−4750.
(13) Baca, S. G.; Filippova, I. G.; Keene, T. D.; Botezat, O.; Malaestean, I. L.; Stoeckli-Evans, H.; Kravtsov, V. C.; Chumacov, I.; Liu, S. X.; Decurtins, S. Iron(III)-Pivalate-Based Complexes with Tetranuclear $\{Fe_4(\mu_3\text{-}O)_2\}^{8+}$ Cores and *N*-Donor Ligands: Formation of Cluster and Polymeric Architectures. *Eur. J. Inorg. Chem.* **2011**, *3*, 356−367.
(14) Tanase, T.; Inagaki, T.; Yamada, Y.; Kato, M.; Ota, E.; Yamazaki, M.; Sato, M.; Mori, W.; Yamaguchi, K.; Mikuriya, M.; Takahashi, M.; Takeda, M.; Kinoshita, I.; Yano, S. Tetranuclear Iron(III) Complexes with Amino Acids Involving a Planar (μ-oxo)(μ-hydroxo)bis(μ-alkoxo)bis(μ-carboxylato)tetrairon Core. *J. Chem. Soc., Dalton Trans.* **1998**, 713−718.
(15) Matsui, M.; Fowler, J. H.; Walling, L. L. Leucine Aminopeptidases: Diversity in Structure and Function. *Biol. Chem.* **2006**, *387*, 1535−1544.
(16) Volbeda, A.; Lahm, A.; Sakiyama, F.; Suck, D. Crystal Structure of Penicillium Citrinum P1 Nuclease at 2.8 Å Resolution. *EMBO J.* **1991**, *10*, 1607−1618.
(17) Twitchett, M. B.; Sykes, A. G. Structure, Properties and Reactivity of the $Fe^{II}Fe^{III}$ and $Zn^{II}Fe^{III}$ Purple Acid Phosphatases. *Eur. J. Inorg. Chem.* **1999**, *1999*, 2105−2115.
(18) Kim, E. E.; Wyckoff, H. W. Reaction Mechanism of Alkaline Phosphatase Based on Crystal Structures. Two-metal Ion Catalysis. *J. Mol. Biol.* **1991**, *218*, 449−464.
(19) Heinz, U.; Adolph, H. W. Metallo-beta-Lactamases: Two Binding Sites for one Catalytic Metal Ion. *Cell. Mol. Life Sci.* **2004**, *61*, 2827−2839.
(20) Schenk, G.; Mitic, N.; Hanson, G. R.; Comba, P. Purple Acid Phosphatase: A Journey into the Function and Mechanism of a Colorful Enzyme. *Coord. Chem. Rev.* **2013**, *257*, 473−482.
(21) Mitic, N.; Smith, S. J.; Neves, A.; Guddat, L. W.; Gahan, L. R.; Schenk, G. The Catalytic Mechanisms of Binuclear Metallohydrolases. *Chem. Rev.* **2006**, *106*, 3338−3363.
(22) Schenk, G.; Guddat, L. W.; Ge, Y.; Carrington, L. E.; Hume, D. A.; Hamilton, S.; De Jersey, J. Identification of Mammalian-like Purple Acid Phosphatases in a Wide Range of Plants. *Gene* **2000**, *250*, 117−125.
(23) Flanagan, J. U.; Cassady, A. I.; Schenk, G.; Guddat, L. W.; Hume, D. A. Identification and Molecular Modeling of a Novel, Plant-like, Human Purple Acid Phosphatase. *Gene* **2006**, *377*, 12−20.
(24) Mitic, N.; Valizadeh, M.; Leung, E. W.; Jersey, J. D.; Hamilton, S.; Hume, D. A.; Cassady, A. I.; Schenk, G. Human Tartarate-Resistant Acid Phosphatase Becomes an Effective ATPase upon Proteolytic Activation. *Arch. Biochem. Biophys.* **2005**, *439*, 154−164.
(25) Oddie, G. W.; Schenk, G.; Angel, N. Z.; Walsh, N.; Guddat, L. W.; De Jersey, J.; Cassady, A. I.; Hamilton, S. E.; Hume, D. A. Structure, Function, and Regulation of Tartrate-Resistant Acid Phosphatase. *Bone* **2000**, *27*, 575−584.
(26) Bozzo, G. G.; Raghothama, K. G.; Plaxton, W. C. Structural and Kinetic Properties of a Novel Purple Acid Phosphatase from Phosphate-starved Tomato (Lycopersicon esculentum) Cell Cultures. *Biochem. J.* **2004**, *377*, 419−428.
(27) Zambelli, B.; Musiani, F.; Benini, S.; Ciurli, S. Chemistry of Ni^{2+} in Urease: Sensing, Trafficking, and Catalysis. *Acc. Chem. Res.* **2011**, *44*, 520−530.
(28) Selleck, C.; Clayton, D.; Gahan, L. R.; Mitic, N.; McGeary, R. P.; Pedroso, M. M.; Guddat, L. W.; Schenk, G. Visualization of the Reaction Trajectory and Transition State in a Hydrolytic Reaction Catalyzed by a Metalloenzyme. *Chem. - Eur. J.* **2017**, *23*, 4778−4781.
(29) Guddat, L. W.; McAlpine, A. S.; Hume, D.; Hamilton, S.; De Jersey, J.; Martin, J. L. Crystal Structure of Mammalian Purple Acid Phosphatase. *Structure* **1999**, *7*, 757−767.
(30) Mitic, N.; Hadler, K. S.; Gahan, L. R.; Hengge, A. C.; Schenk, G. The Divalent Metal Ion in the Active Site of Uteroferrin Modulates Substrate Binding and Catalysis. *J. Am. Chem. Soc.* **2010**, *132*, 7049−7054.
(31) Patra, A.; Sen, T. K.; Ghorai, A.; Musie, G. T.; Mandal, S. K.; Ghosh, U.; Bera, M. Synthesis, Structure, Spectroscopic Characterization, and Protein Binding Affinity of New Water-Soluble Hetero- and Homometallic Tetranuclear $[Cu^{II}_2Zn^{II}_2]$ and $[Cu^{II}_4]$ Clusters. *Inorg. Chem.* **2013**, *52*, 2880−2890.
(32) Patra, A.; Saha, S. K.; Sen, T. K.; Carrella, L.; Musie, G. T.; Khuda-Bukhsh, A. R.; Bera, M. Water-Soluble Heteronuclear $[NaCu^{II}_6]$ Metallomacrocyclic Sandwich Complexes: Synthesis, Structure, Properties and In Vitro Biological Studies. *Eur. J. Inorg. Chem.* **2014**, *30*, 5217−5232.
(33) Giri, G. C.; Patra, A.; Vijaykumar, G.; Carrella, L.; Bera, M. Hydrolytically Active Tetranuclear $[Ni^{II}_2]_2$ Complexes: Synthesis, Structure, Spectroscopy and Phosphoester Hydrolysis. *RSC Adv.* **2015**, *5*, 99270−99283.
(34) Haldar, S.; Patra, A.; Vijaykumar, G.; Carrella, L.; Bera, M. Dinuclear and Tetranuclear Complexes of Copper Coordinated by an Anthracene-Based New μ-bis(tridentate) Ligand: Synthesis, Structure, Spectroscopy and Magnetic Properties. *Polyhedron* **2016**, *117*, 542−551.
(35) Haldar, S.; Vijaykumar, G.; Carrella, L.; Batha, S.; Musie, G. T.; Bera, M. Inorganic Phosphate and Arsenate within New Tetranuclear Copper and Zinc Complexes: Syntheses, Crystal Structures, Magnetic, Electrochemical, and Thermal Studies. *ACS Omega* **2017**, *2*, 1535−1549.
(36) Bera, M.; Musie, G. T.; Powell, D. R. Synthesis and Characterization of New Mono- and Heptazinc Complexes with Unusual Amide Coordination Modes. *Inorg. Chem.* **2009**, *48*, 4625−4627.
(37) Jameson, D. L.; Xie, C. L.; Hendrickson, D. N.; Potenza, J. A.; Schugar, H. J. Molecular Structure and Magnetic Properties of a Novel Fe(III) Tetranuclear Complex Containing Oxo, Alkoxo, and Carbonato Bridges. *J. Am. Chem. Soc.* **1987**, *109*, 740−746.
(38) Frischmann, P. D.; Gallant, A. J.; Chong, J. H.; MacLachlan, M. J. Zinc Carboxylate Cluster Formation in Conjugated Metallomacrocycles: Evidence for Templation. *Inorg. Chem.* **2008**, *47*, 101−112.
(39) Patra, A.; Haldar, S.; Vijaykumar, G.; Carrella, L.; Ghosh, A. K.; Bera, M. New Symmetrical Dinucleating Ligand Based Assembly of Bridged Dicopper(II) and Dizinc(II) Centers: Synthesis, Structure, Spectroscopy, Magnetic Properties and Glycoside Hydrolysis. *Inorg. Chim. Acta* **2015**, *436*, 195−204.
(40) West, A. R. *Solid State Chemistry and Its Applications*; Wiley: Chichester, U.K., 1984; pp 553−560.
(41) Bain, G. A.; Berry, J. F. Diamagnetic Corrections and Pascal's Constants. *J. Chem. Educ.* **2008**, *85*, 532−536.
(42) Panasci, A. F.; Ohlin, C. A.; Harley, S. J.; Casey, W. H. Rates of Water Exchange on the $[Fe_4(OH)_2(hpdta)_2(H_2O)_4]^0$ Molecule and Its Implications for Geochemistry. *Inorg. Chem.* **2012**, *51*, 6731−6738.
(43) Tan, X. W.; Wang, B. M.; Wang, Y.; Zhan, S. Z. Design, Synthesis, Structure and Magnetic Behavior of a High Spin Binuclear Fe(III) Complex of N-(1-ethanol)-N,N-bis(3-tert-butyl-5-methyl-2-hydroxybenxyl) Amine. *Inorg. Chem. Commun.* **2010**, *13*, 1061−1063.
(44) Shin, J. W.; Bae, J. M.; Kim, C.; Min, K. S. Catalysis and Molecular Magnetism of Dinuclear Iron(III) Complexes with N-(2-pyridylmethyl)iminodiethanol/-ate. *Dalton Trans.* **2014**, *43*, 3999−4008.
(45) Armstrong, W. H.; Lippard, S. J. Reversible Protonation of the Oxo Bridge in a Hemerythrin Model Compound. Synthesis, Structure, and Properties of (p-Hydroxo)bis(p-acetate)- bis[hydrotris(1-pyrazolyl) borato]diiron(III), $[(HB(pz)_3)Fe(OH)(O_2CCH_3)_2Fe(HB(pz)_3)]^+$. *J. Am. Chem. Soc.* **1984**, *106*, 4632−4633.
(46) Biswas, B.; Mitra, M.; Adhikary, J.; Krishna, G. R.; Bag, P. P.; Reddy, C. M.; Aliaga-Alcalde, N.; Chattopadhyay, T.; Das, D.; Ghosh, R. Synthesis, X-ray Structural and Magnetic Characterizations, and Epoxidation Activity of a New bis(l-acetato)(l-alkoxo)dinuclear Iron(III) Complex. *Polyhedron* **2013**, *53*, 264−268.
(47) Kato, M.; Yamada, Y.; Inagaki, T.; Mori, W.; Sakai, K.; Tsubomura, T.; Sato, M.; Yano, S. Structures and Magnetic Properties

DOI: 10.1021/acs.inorgchem.8b01441
Inorg. Chem. XXXX, XXX, XXX−XXX

of Iron(III) Dinuclear Complexes with Alkoxo and Carboxylato Bridges. *Inorg. Chem.* **1995**, *34*, 2645−2651.
(48) (a) Deacon, G. B.; Phillips, R. Relationships between the Carbon-Oxygen Stretching Frequencies of Carboxylato Complexes and the Type of Carboxylate Coordination. *Coord. Chem. Rev.* **1980**, *33*, 227−250. (b) Nakamoto, K. *Infrared and Raman Spectra of Inorganic and Coordination Compounds*, 4th ed.; Wiley: New York, 1986; pp 231−233, 251, 253.
(49) Tanase, T.; Inoue, C.; Ota, E.; Yano, S.; Takahashi, M.; Takeda, M. Tetranuclear Iron(III) Complexes with a Planar (μ-oxo)(μ-hydroxo)bis(μ-alkoxo)bis(μ-carboxylato) Tetrairon Core Derived from Hydrolysis of Carboxylic Acid Amides by Diiron(III) Center. *Inorg. Chim. Acta* **2000**, *297*, 18−26.
(50) Westerheide, L.; Muller, F. K.; Than, R.; Krebs, B. Syntheses and Structural Characterization of Dinuclear and Tetranuclear Iron(III) Complexes with Dinucleating Ligands and their Reactions with Hydrogen Peroxide. *Inorg. Chem.* **2001**, *40*, 1951−1961.
(51) Duboc-Toia, C.; Menage, S.; Vincent, J. M.; Averbuch-Pouchot, M. T.; Fontecave, M. Structure of a (μ-Oxo)(dihydroxo)diiron(III) Complex and Its Reactivity toward Phosphodiesters. *Inorg. Chem.* **1997**, *36*, 6148−6149.
(52) MacBeth, C. E.; Gupta, R.; Mitchell-Koch, K. R.; Young, V. G.; Lushington, G. H., Jr; Thompson, W. H.; Hendrich, M. P.; Borovik, A. S. Utilization of Hydrogen Bonds to Stabilize M-O(H) Units: Synthesis and Properties of Monomeric Iron and Manganese Complexes with Terminal Oxo and Hydroxo Ligands. *J. Am. Chem. Soc.* **2004**, *126*, 2556−2567.
(53) Gkioni, C.; Boudalis, A. K.; Sanakis, Y.; Psycharis, V.; Raptopoulou, C. P. 2-Pyridyl Ketone Oximes in Iron(III) Carboxylate Chemistry: Synthesis, Structural and Physical Studies of Tetranuclear Clusters Containing the $[Fe_4(\mu_3\text{-}O)_2]^{8+}$ 'butterfly' core. *Polyhedron* **2009**, *28*, 3221−3226.
(54) Boskovic, C.; Sieber, A.; Chaboussant, G.; Gudel, H. U.; Ensling, J.; Wernsdorfer, W.; Neels, A.; Labat, G.; Stoeckli-Evans, H.; Janssen, S. Synthesis and Characterization of a New Family of Bi-, Tri-, Tetra-, and Pentanuclear Ferric Complexes. *Inorg. Chem.* **2004**, *43*, 5053−5068.
(55) Grimme, S. Do Special Noncovalent $\pi-\pi$ Stacking Interactions Really Exist. *Angew. Chem., Int. Ed.* **2008**, *47*, 3430−3434.
(56) Matthews, R. P.; Welton, T.; Hunt, P. A. Competitive pi Interactions and Hydrogen Bonding within Imidazolium Ionic Liquids. *Phys. Chem. Chem. Phys.* **2014**, *16*, 3238−3253.
(57) Waters, M. L. Aromatic Interactions in Model Systems. *Curr. Opin. Chem. Biol.* **2002**, *6*, 736−741.
(58) Addison, A.; Rao, T. N.; Reedijk, J.; van Rijn, J.; Verschoor, G. C. Synthesis, Structure, and Spectroscopic Properties of Copper(II) Compounds Containing Nitrogen-Sulphur Donor Ligands; The Crystal and Molecular Structure of Aqua[1,7- bis(*N*-methylbenzimidazol-2′-yl)-2,6-dithiaheptane] Copper(II) Perchlorate. *J. Chem. Soc., Dalton Trans.* **1984**, 1349−1356.
(59) Curtiss, A. B. S.; Bera, M.; Musie, G. T.; Powell, D. R. Synthesis and Characterization of Mono- and μ_6-sulfato Hexanuclear Zinc Complexes of a New Symmetric Dinucleating Ligand. *Dalton Trans.* **2008**, 2717−2724.
(60) Chen, X. Q.; Peng, X. J.; Wang, J. Y.; Wang, Y.; Wu, S.; Zhang, L. Z.; Wu, T.; Wu, Y. K. Efficient Increase of DNA Cleavage Activity of a Diiron(III) Complex by a Conjugating Acridine Group. *Eur. J. Inorg. Chem.* **2007**, *2007*, 5400−5407.
(61) Kantacha, A.; Buchholz, R.; Smith, S. J.; Schenk, G.; Gahan, L. R. Phosphate Ester Cleavage Promoted by a Tetrameric Iron(III) Complex. *JBIC, J. Biol. Inorg. Chem.* **2011**, *16*, 25−32.
(62) Bosch, S.; Comba, P.; Gahan, L. R.; Schenk, G. Dinuclear Zinc(II) Complexes with Hydrogen Bond Donors as Structural and Functional Phosphatase Models. *Inorg. Chem.* **2014**, *53*, 9036−9051.
(63) Mendes, L. L.; Englert, D.; Fernandes, C.; Gahan, L. R.; Schenk, G.; Horn, A., Jr Metallohydrolase Biomimetics with Catalytic and Structural Flexibility. *Dalton Trans.* **2016**, *45*, 18510−18521.
(64) Mancin, F.; Tecilla, P. Zinc (II) Complexes as Hydrolytic Catalysts of Phosphate Diester Cleavage: From Model Substrates to Nucleic Acids. *New J. Chem.* **2007**, *31*, 800−817.
(65) Morrow, J. R.; Iranzo, O. Synthetic Metallonucleases for RNA Cleavage. *Curr. Opin. Chem. Biol.* **2004**, *8*, 192−200.
(66) Greatti, A.; Scarpellini, M.; Peralta, R. A.; Casellato, A.; Bortoluzzi, A. J.; Xavier, F. R.; Jovito, R.; de Brito, M. A.; Szpoganicz, B.; Tomkowicz, Z.; Rams, M.; Haase, W.; Neves, A. Synthesis, Structure, and Physicochemical Properties of Dinuclear NiII Complexes as Highly Efficient Functional Models of Phosphohydrolases. *Inorg. Chem.* **2008**, *47*, 1107−1119.
(67) Comba, P.; Gahan, L. R.; Mereacre, V.; Hanson, G. R.; Powell, A. K.; Schenk, G.; Zajaczkowski-Fischer, M. Spectroscopic Characterization of the Active $Fe^{III}Fe^{III}$ and $Fe^{III}Fe^{II}$ Forms of a Purple Acid Phosphatase Model System. *Inorg. Chem.* **2012**, *51*, 12195−12209.
(68) Silva, G. A. D. S.; Amorim, A. L.; Souza, B. D.; Gabriel, P.; Terenzi, H.; Nordlander, E.; Neves, A.; Peralta, R. A. Synthesis and Characterization of $Fe^{III}(\mu\text{-}OH)Zn^{II}$ Complexes: Effects of a Second Coordination Sphere and Increase in the Chelate Ring Size on the Hydrolysis of a Phosphate Diester and DNA. *Dalton Trans.* **2017**, *46*, 11380−11394.
(69) Chen, J.; Wang, X.; Zhu, Y.; Lin, J.; Yang, X.; Li, Y.; Lu, Y.; Guo, Z. An Asymmetric Dizinc Phosphodiesterase Model with Phenolate and Carboxylate Bridges. *Inorg. Chem.* **2005**, *44*, 3422−3430.
(70) Buchholz, R. R.; Etienne, M. E.; Dorgelo, A.; Mirams, R. E.; Smith, S. J.; Chow, S. Y.; Hanton, L. R.; Jameson, G. B.; Schenk, G.; Gahan, L. R. A Structural and Catalytic Model for Zinc Phosphoesterases. *Dalton Trans.* **2008**, 6045−6054.
(71) Bernhardt, P. V.; Bosch, S.; Comba, P.; Gahan, L. R.; Hanson, G. R.; Mereacre, V.; Noble, C. J.; Powell, A. K.; Schenk, G.; Wadepohl, H. An Approach to More Accurate Model Systems for Purple Acid Phosphatases (PAPs). *Inorg. Chem.* **2015**, *54*, 7249−7263.
(72) Pathak, C.; Gangwar, M. K.; Ghosh, P. Homodinuclear [Fe(III)-Fe(III)] and [Zn(II)-Zn(II)] Complexes of a Binucleating $[N_4O_3]$ Symmetrical Ligand with Purple Acid Phosphatase (PAP) and Zinc Phosphoesterase Like Activity. *Polyhedron* **2018**, *145*, 88−100.
(73) Peralta, R. A.; Bortoluzzi, A. J.; de Souza, B.; Jovito, R.; Xavier, F. R.; Couto, R. A. A.; Casellato, A.; Nome, F.; Dick, A.; Gahan, L. R.; Schenk, G.; Hanson, G. R.; De Paula, F. C. S.; Pereira-Maia, E. C.; de Machado, S. P.; Severino, P. C.; Pich, C.; Bortolotto, T.; Terenzi, H.; Castellano, E. E.; Neves, A.; Riley, M. J. Electronic Structure and Spectro-Structural Correlations of $Fe^{III}Zn^{II}$ Biomimetics for Purple Acid Phosphatases: Relevance to DNA Cleavage and Cytotoxic Activity. *Inorg. Chem.* **2010**, *49*, 11421−11438.
(74) Dalle, K. E.; Daumann, L. J.; Schenk, G.; McGeary, R. P.; Hanton, L. R.; Gahan, L. R. Ligand Modifications Modulate the Mechanism of Binuclear Phosphatase Biomimetics. *Polyhedron* **2013**, *52*, 1336−1343.
(75) Boudalis, A. K.; Aston, R. E.; Smith, S. J.; Mirams, R. E.; Riley, M. J.; Schenk, G.; Blackman, A. G.; Hantonc, L. R.; Gahana, L. R. Synthesis and Characterization of the Tetranuclear Iron(III) Complex of a New Asymmetric Multidentate Ligand. A Structural Model for Purple Acid Phosphatases. *Dalton Trans.* **2007**, 5132−5139.
(76) Mochizuki, K.; Ishima, Y.; Hayano, K. Synthesis and Structures of Zinc Complexes With New Binucleating Ligands Containing Alkoxide Bridges, and their Activities in the Hydrolysis of tris(p-nitrophenyl)-phosphate. *Inorg. Chim. Acta* **2009**, *362*, 2722−2727.
(77) Daumann, L. J.; Dalle, K. E.; Schenk, G.; McGeary, R. P.; Bernhardt, P. V.; Ollis, D. L.; Gahan, L. R. The Role of Zn-OR and Zn-OH Nucleophiles and the Influence of *para*-Substituents in the Reactions of Binuclear Phosphatase Mimetics. *Dalton Trans.* **2012**, *41*, 1695−1708.
(78) Daumann, L. J.; Schenk, G.; Ollis, D. L.; Gahan, L. R. Spectroscopic and Mechanistic Studies of Dinuclear Metallohydrolases and their Biomimetic Complexes. *Dalton Trans.* **2014**, *43*, 910−928.
(79) Brown, J. J.; Gahan, L. R.; Schöffler, A.; Krenske, E. H.; Schenk, G. Investigation of the Identity of the Nucleophile Initiating the Hydrolysis of Phosphate Esters Catalyzed by Dinuclear Mimics of Metallohydrolases. *J. Inorg. Biochem.* **2016**, *162*, 356−365.
(80) Bates, R. G.; Paabo, M.; Robinson, R. A. Interpretation of pH Measurements in Alcoho-Water Solvents. *J. Phys. Chem.* **1963**, *67*, 1833−1838.

DOI: 10.1021/acs.inorgchem.8b01441
Inorg. Chem. XXXX, XXX, XXX−XXX

(81) (a) Gans, P.; Sabatini, A.; Vacca, A. Investigation of Equilibria in Solution. Determination of Equilibrium Constants with the HYPERQUAD Suite of Programs. *Talanta* **1996**, *43*, 1739−1753. (b) Alderighi, P.; Gans, A.; Ienco, D.; Peters, A. S.; Vacca, A. Hyperquad Simulation and Speciation (HySS): A Utility Program for the Investigation of Equilibria Involving Soluble and Partially Soluble Species. *Coord. Chem. Rev.* **1999**, *184*, 311−318.
(82) Albedyhl, S.; Averbuch-Pouchot, M. T.; Belle, C.; Krebs, B.; Pierre, J. L.; Aman, E. S.; Torelli, S. Dinuclear Zinc(II)-Iron(III) and Iron(II)-Iron(III) Complexes as Models for Purple Acid Phosphatases. *Eur. J. Inorg. Chem.* **2001**, *2001*, 1457−1464.
(83) Sheldrick, G. M. *SADABS. Program for Multi-Scan Absorption Correction of Area Detector Data*; University of Göttingen, Germany, 2002.
(84) Altomare, A.; Burla, M. C.; Camalli, M.; Cascarano, G. L.; Giacovazzo, C.; Guagliardi, A.; Moliterni, A. G. G.; Polidori, G.; Spagna, R. *SIR-97*: A New Tool for Crystal Structure Determination and Refinement. *J. Appl. Crystallogr.* **1999**, *32*, 115−119.
(85) Sheldrick, G. M. Crystal Structure Refinement with SHELXL. *Acta Crystallogr., Sect. C: Struct. Chem.* **2015**, *C71*, 3−8.
(86) *International Tables for Crystallography*, Vol C, Tables 6.1.1.4, 4.2.6.8, and 4.2.4.2; Kluwer: Boston, 1995.
(87) Dolomanov, O. V.; Bourhis, L. J.; Gildea, R. J.; Howard, J. A. K.; Puschmann, H. OLEX2: A Complete Structure Solution, Refinement and Analysis Program. *J. Appl. Crystallogr.* **2009**, *42*, 339−341.
(88) Frisch, M. J.; Trucks, G. W.; Schlegel, H. B.; Scuseria, G. E.; Robb, M. A.; Cheeseman, J. R.; Montgomery, J. A.; Vreven, Jr., T.; Kudin, K. N.; Burant, J. C.; Millam, J. M.; Iyengar, S. S.; Tomasi, J.; Barone, V.; Mennucci, B.; Cossi, M.; Scalmani, G.; Rega, N.; Petersson, G. A.; Nakatsuji, H.; Hada, M.; Ehara, M.; Toyota, K.; Fukuda, R.; Hasegawa, J.; Ishida, M.; Nakajima, T.; Honda, Y.; Kitao, O.; Nakai, H.; Klene, M.; Li, X.; Knox, J. E.; Hratchian, H. P.; Cross, J. B.; Adamo, C.; Jaramillo, J.; Gomperts, R.; Stratmann, R. E.; Yazyev, O.; Austin, A. J.; Cammi, R.; Pomelli, C.; Ochterski, J. W.; Ayala, P. Y.; Morokuma, K.; Voth, G. A.; Salvador, P.; Dannenberg, J. J.; Zakrzewski, V. G.; Dapprich, S.; Daniels, A. D.; Strain, M. C.; Farkas, O.; Malick, D. K.; Rabuck, A. D.; Raghavachari, K.; Foresman, J. B.; Ortiz, J. V.; Cui, Q.; Baboul, A. G.; Clifford, S.; Cioslowski, J.; Stefanov, B. B.; Liu, G.; Liashenko, A.; Piskorz, P.; Komaromi, I.; Martin, R. L.; Fox, D. J.; Keith, T.; Al-Laham, M. A.; Peng, C. Y.; Nanayakkara, A.; Challacombe, M.; Gill, P. M. W.; Johnson, B.; Chen, W.; Wong, M. W.; Gonzalez, C.; Pople, J. A. *Gaussian 03*, Revision A.1; Gaussian, Inc.: Pittsburgh, PA, 2003.
(89) Becke, A. D. Density-Functional Exchange-Energy Approximation with Correct Asymptotic Behavior. *Phys. Rev. A: At., Mol., Opt. Phys.* **1988**, *38*, 3098−3100.
(90) Becke, A. D. Density-Functional Thermochemistry III: The Role of Exact Exchange. *J. Chem. Phys.* **1993**, *98*, 5648−5652.
(91) Lee, C.; Yang, W.; Parr, R. G. Development of the Colle-Salvetti Correlation-Energy Formula into a Functional of the Electron Density. *Phys. Rev. B: Condens. Matter Mater. Phys.* **1988**, *37*, 785−789.
(92) Ditchfield, R.; Hehre, W. J.; Pople, J. A. Self-Consistent Molecular-Orbital Methods. IX. An Extended Gaussian-Type Basis for Molecular-Orbital Studies of Organic Molecules. *J. Chem. Phys.* **1971**, *54*, 724−728.
(93) Hehre, W. J.; Ditchfield, R.; Pople, J. A. Self-Consistent Molecular Orbital Methods. XII. Further Extensions of Gaussian-Type Basis Sets for Use in Molecular Orbital Studies of Organic Molecules. *J. Chem. Phys.* **1972**, *56*, 2257−2261.

DOI: 10.1021/acs.inorgchem.8b01441
Inorg. Chem. XXXX, XXX, XXX−XXX